Free Falling of Spheres in a Quiescent Fluid

Siavash Hedayati Nasab

A Thesis

in

The Department

of

Mechanical, Industrial, and Aerospace Engineering

Presented in Partial Fulfillment of the Requirements

for the Degree of

Master of Applied Science (Mechanical Engineering) at

Concordia University

Montréal, Québec, Canada

September 2017

CONCORDIA UNIVERSITY

School of Graduate Studies

This is to certify that the thesis prepared

By: **Siavash Hedayati Nasab**

Entitled: **Free Falling of Spheres in a Quiescent Fluid**

and submitted in partial fulfillment of the requirements for the degree of

Master of Applied Science (Mechanical Engineering)

complies with the regulations of this University and meets the accepted standards with respect to originality and quality.

Signed by the Final Examining Committee:

_____ Chair
Dr. Ida Karimfazli

_____ External Examiner
Dr. Samuel Li

_____ Examiner
Dr. Hoi Dick Ng

_____ Supervisor
Dr. Georgios H. Vatistas

_____ Co-supervisor
Dr. Brian Vermeire

Approved by _____
Martin D. Pugh, Chair
Department of Mechanical, Industrial, and Aerospace Engineering

_____ 2017

_____
Amir Asif, Dean
Faculty of Engineering and Computer Science

Abstract

Free Falling of Spheres in a Quiescent Fluid

Siavash Hedayati Nasab

Motion of spheres falling through fluids is a classical problem in fluid mechanics. The problem is solved for steady motion and other special cases such as for small and large Reynolds numbers, but not yet for transitional flows due to a complicated nonlinear drag relationship. However, in recent decades a new approach has become available for studying this problem via the development of powerful processors and computers. In this thesis we investigate free falling of spherical shape objects through fluid media. We produce experimental data and then model the motion mathematically via Newton's second law and the Navier-Stokes equations. The resulting second order non-linear differential equation has been solved numerically. Finally, by using the fluid-structure interaction method (immersed boundary method) we simulate the free fall of spheres in water and compare these results with our experimental data. The aim of this study will be to answer how density, viscosity, temperature and gravitational acceleration affect the rate of descent of a solid body through a fluid.

"Oh, threats of Hell and Hopes of Paradise!
One thing at least is certain–This Life flies;
One thing is certain and the rest is Lies;
The Flower that once has blown for ever dies. ."

Omar Khayyam

Acknowledgments

I would like to express my sincere gratitude to my co-supervisor Doctor Georgios H.Vatistas for his continuous support during my study and research, for his patience, motivation, enthusiasm, and immense knowledge. His guidance helped me throughout the research and writing of this thesis.

I would also like to acknowledge my co-supervisor Doctor Brian Vermeire,The door to his office was always open whenever I ran into a trouble or had a question about my research or writing.

Last but not least, I would like to thanks my parents, who have always been there for me when I needed them. Their love provided my inspiration and was my driving force. I owe them everything I have and I wish I could show them just how much I love and appreciate them. I will be grateful forever for their love and their support.

Contents

List of Figures

List of Tables

Nomenclature

δ_{ij}	Kronecker delta
μ	Dynamic viscosity
ν	Kinematic viscosity
ρ	Density
ρ_f	Fluid density
ρ_w	Water density
C_D	Drag coefficient
CFD	Computational Fluid Dynamics
D	Drag force
DNS	Direct Numerical Simulation
FSI	Fluid-Structure Interaction
LES	Large Eddy Simulation
LHS	Left Hand Side
m_f	Fluid mass
m_p	Particle mass
p	Pressure

$RANS$ Reynolds Averaged Navier Stokes

Re Reynolds number

RHS Right Hand Side

t Time

V Velocity

Chapter 1

Introduction

1.1 History of free fall studies

We have all observed objects in free fall. This classical problem in physics has attracted attention since the earliest days of science. History books tell us that before the sixteenth century. It was generally assumed that the acceleration of a falling body would be proportional to its mass. The ancient Greek philosopher Aristotle (384-322 BC) [1] wrote this law in what is considered to be the first book on mechanics. Philoponous (490 – 570 AD) [2] [3] followed by Stevin (1548–1620) [4] and later on by Galileo Galilei (1564 -1641) [5] expressed some objections about Aristotle's assertion. However, Steven and Galileo Galilei (1564 - 1641) [5] were the first modern scientists who put Aristotle's theories to the test. Unlike others before him, Galileo tried to verify his own theories through experimentation and observation. He combined the results of these experiments with mathematical analysis in a method that was novel in those times. He demonstrated that pairs of objects of the same shapes but different masses dropped from the top of the famous tower of Pisa touched the ground simultaneously with the same velocity and acceleration. Nevertheless, Galileo's observations seemed unintuitive, because we observe that on earth, heavier objects hit the ground earlier than lighter ones.

Later, reliable measurements and experiments showed that the velocity of objects with

different masses, sizes, and materials, dropped simultaneously from the same height, are different once they reached the ground. Accurate experiments also proved that the effect of mass on the velocity of objects of similar shapes and sizes is very small, and this effect tended to decrease with lowering the release height and tended to increase with increasing the release height [5]. However, this difference no longer increased by increasing the release height more than a specific value, which is proportional to the mass and shape of the object and the viscosity of the fluid through which it falls. This is due to the object reaching its terminal velocity. In fact, experimental observations showed that in more viscous fluids, such as water, an object reaches its terminal velocity earlier.

In the eighteenth century, fluid mechanics contributed modeling to this classical problem. The drag force, defined as a force acting in the opposite direction of the relative motion of an object, is affected by cross-sectional surface area and surface smoothness. In other words, drag force is a resistive force acting on a solid body moving through a fluid. Significant experimental and analytical progress has been made studying drag force, and it is now known that any object dropped in a fluid media starts accelerating and then reaches its steady state (terminal velocity). Meanwhile, via progress in numerical methods and computational power a new approach for studying the phenomena has been introduced, Computational Fluid Dynamics (CFD) [6].

1.2 Why free fall is important?

Free fall is a common phenomenon observed in our daily lives. However, free fall in a viscous fluid has a complicated nonlinear behaviour with a number of physical and industrial applications. Hydrodynamic or aerodynamic forces during the simple free fall of a sphere can be observed in a wide range of other phenomena in nature from multiphase flow to the aerospace and naval industries. In fact, free fall is a simple example of moving solid particles or even gas bubbles through a fluid. Motion of gas bubbles and rigid particles in a fluid is widely observed in industry, from the oil and petrochemical industries to the

aerospace industry. Hence it can be said that free fall is a classical problem with a variety of applications. In Figure 1.1 blades of a boat propeller can be seen with small solid objects pitting on its surface (cavitation). In Figure 1.2 Russia's Urals region has been rocked by a meteorite explosion. The impact wave damaged several buildings, and destroyed thousands of windows.

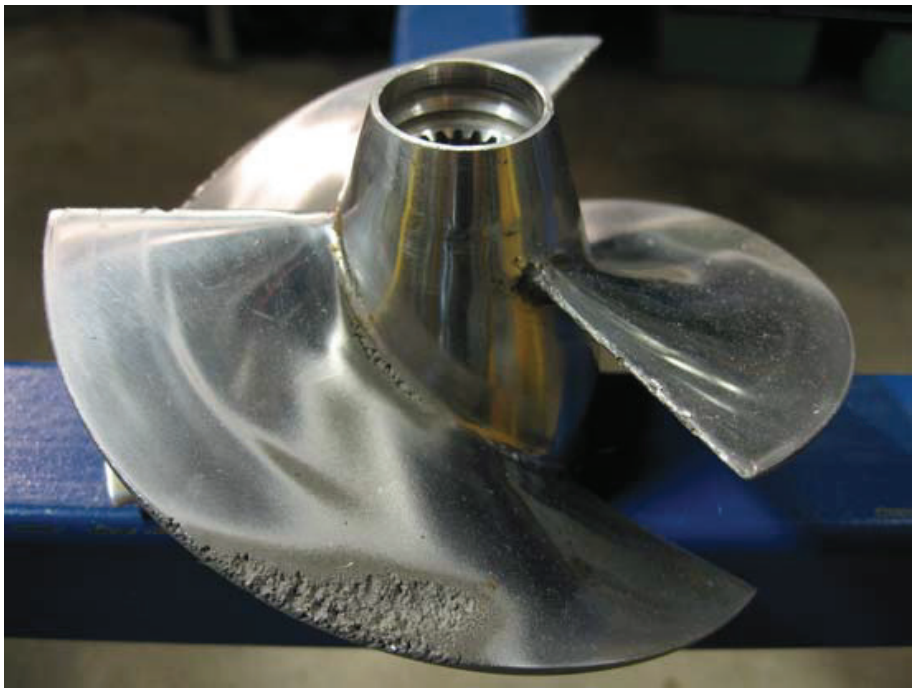

Figure 1.1: Cavitation of small solid objects on blades of a boat propeller [7]

Figure 1.2: Russia's Urals region rocked by a meteor [8]

1.3 On the physics of free fall

Based on Newton's second law and conservation of mass, as an object falls through a viscous fluid its interactions with that fluid are described by the Navier-Stokes equations. There are two types of forces imparted on the solid object by the fluid, pressure forces and shear stress (viscous) forces. However, based on Newton's second law (assuming a rigid body) there are additional forces acting on the object. There is the force of gravity that pulls the sphere downward through the fluid, and based on Archemide's principle, there is a buoyancy force which arises from the fact that fluid pressure increases with depth and this increased pressure is exerted in all directions (Pascal's principle) so that there is an unbalanced upward force on the bottom of a submerged (immersed) object [9] [10]. There is also another apparent force due to the transient terms in the Navier-Stokes equations which is the added or virtual mass. The added mass force can be explained as the required force to accelerate fluid particles around the object, in other words when the solid object wants to accelerate due to viscous effects some fluid particles also accelerate with the solid object so they add to the real mass which is moving and, consequently, a greater force is needed for the acceleration of the particle.

There are also some other minor forces such as the pressure gradient (which is due to difference in the hydrostatic pressure of the fluid surrounding different parts of the object) and the Basset or history force (which addresses lagging of the boundary layer when the solid particle is accelerating). All these force will be discussed in Chapter 3 in detail.

Figure 1.3 shows the idealized major forces in free fall under uniform acceleration of gravity. In this figure, we see that gravity and buoyancy are always aligned with the direction of x-axis by definition. Furthermore, by definition the drag force is parallel to, and in the opposite direction of the velocity vector. In Figure 1.3 we show the velocity vector aligned with the positive x axis, as we expect this to predominantly be the case. However, in practice transverse forces could introduce additional velocity components, misaligning the velocity vector from the x axis.

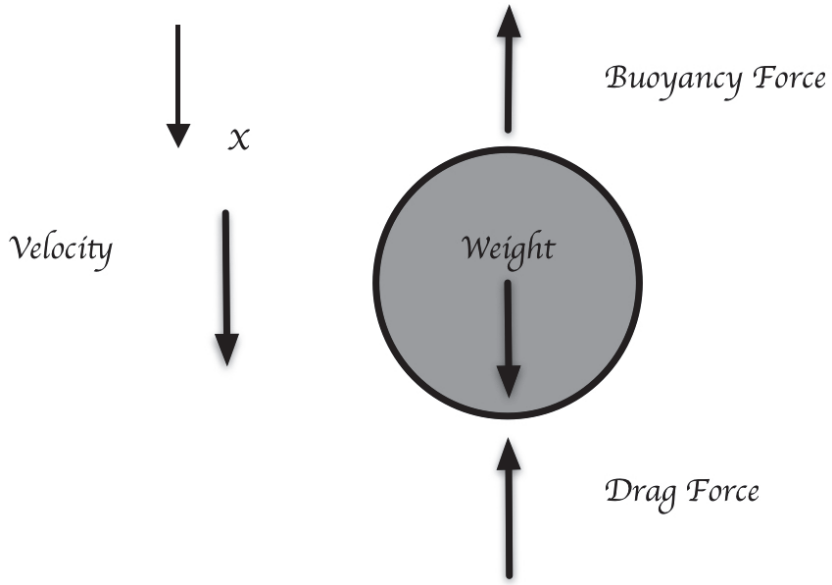

Figure 1.3: Major forces in free fall with Idealized directions

1.4 How to approach to free fall problem

Understanding the motion of a solid object in a viscous fluid remains a fundamental question in multiphase flow modeling. This problem has many engineering applications, such as spray combustion, pollution control, boiling and bubble dynamics, sedimentation, and erosion of turbine blades. These problems are concerned with the interaction of particles with fluids, which requires accurate knowledge of this phenomena.
There are three different possible approaches to addressing this problem in engineering:

- Experimental approaches using motion capturing methods such as the Particle Image Velocimetry (PIV).
- Studying the hydrodynamic forces acting on solid particle using rigid body dynamics to obtain an equation of motion based on Newton's second law.
- Studying the full fluid domain by taking advantage of computational fluid dynamics

All of these approaches are studied in this thesis, and will be discussed in their relevent

chapters.

1.5 Computational fluid dynamics in free fall

1.5.1 CFD and the finite volume method

Numerical approximations to the solution of the mathematical equations describing fluid flow and heat transfer have been an ongoing pursuit for mathematicians and engineers. However, via the development of powerful processors and super computers this approach has become practical. Computational fluid dynamics is one of the tools (in addition to experimental and theoretical methods) that is useful for solving fluid-dynamics problems. Through ongoing improvements of computer hardware, computational fluid dynamics is now applied in many diverse fields including engineering, physics, and meteorology.

In computational fluid dynamics we discretize the fluid domain by generating meshes and transform our nonlinear or linear partial differential equations to coupled algebraic equations [6]. Discretization consists of a process whereby the domain is subdivided into elements and the equations are expressed in discrete form at each element by using finite differences or finite volumes. The finite difference method requires a structured grid arrangement (that is, an organized set of points formed by the intersections of the lines of a boundary-conforming curvilinear coordinate system). However the finite volume method is more flexible and can be formulated to use both structured and unstructured grids (that is, a collection of irregular elements).

Improper assumptions and discretization in turbulent flows could yield inaccuracies in the numerical solution. In order to avoid this, there are a variety of approaches for modelling turbulent flows. The Reynolds-Averaged Navier-Stokes (RANS) equations are derived by decomposing the velocity into time-average and time-fluctuating components [11]. Another approach is large-eddy simulation, which solves the spatially filtered Navier-Stokes equations [11]. The third approach, to simulate turbulent flows is direct numerical simulation, which solves the Navier-Stokes equations on a mesh that is fine enough to resolve

all length scales in the turbulent flow. Unfortunately, direct numerical simulation (DNS) is typically limited to simple geometries and low-Reynolds-number flows because of the limited compute capabilities of even the most powerful modern supercomputers.

The final step in computational fluid dynamics is to visualize the results of the simulation. Visualization enables us to generate velocity vectors, pressure and velocity contours, streamlines, calculation of secondary quantities (such as vorticity), and animations of unsteady flows. Nowadays, we have access to very powerful graphical hardware, but simulating three dimensional transient flows is still difficult. However, we can still obtain valuable data from the approximate equations of RANS and LES.

In this study, with respect to our use case, our geometry, and the availability of computational methods, we decided to use finite volume method to discretize the problem via the CFD solver package ANSYS CFX [12]. There are other approaches such as finite difference schemes, for this special case since the geometry is simple. However, an approach that could be generalized to any geometry, motivated us to use an unstructured finite volume solver.

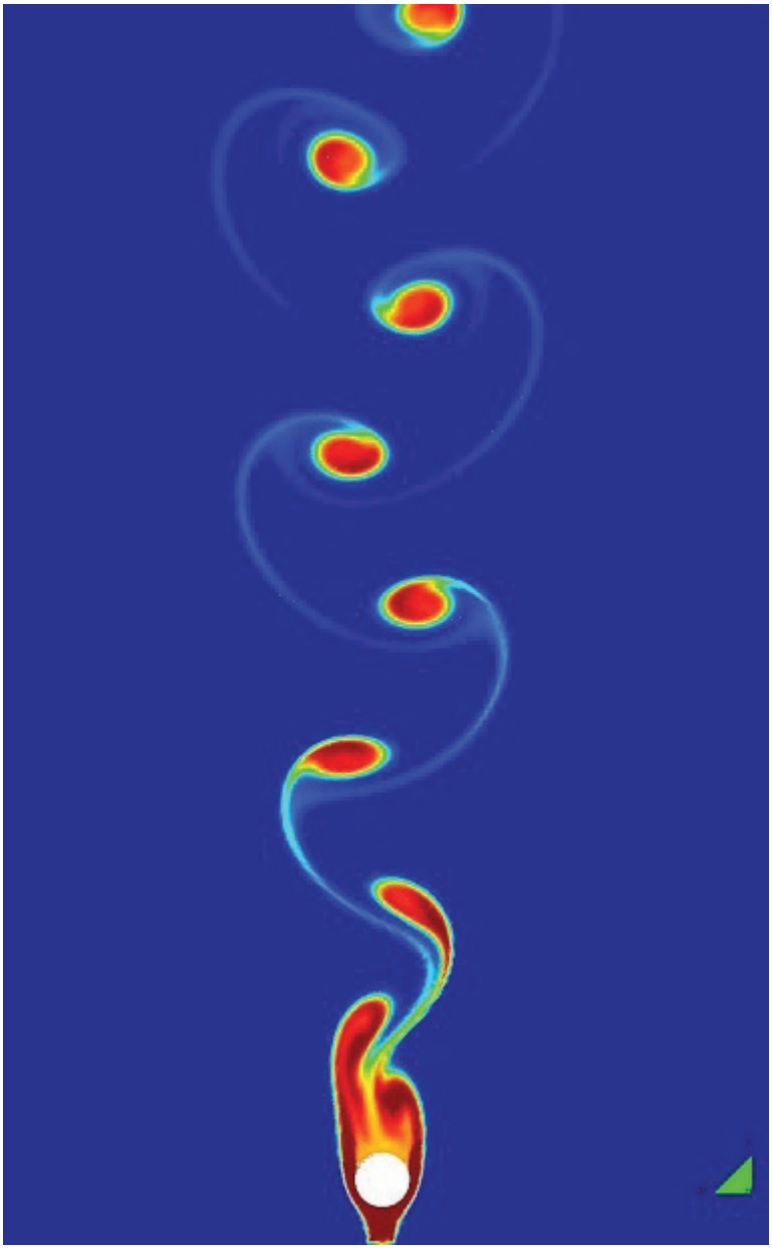

Figure 1.4: Computational fluid dynamics simulation of vortices around a falling sphere

1.6 Thesis objectives

In this thesis, we exploit recent advances in numerical methods and turbulence modeling to study the free fall of spherical shaped objects with three different materials in quiescent water. We provide the results of experimental, numerical, and CFD studies (see Figure 1.4)

and then we compare the results from all three approaches. The effect of drag, buoyancy and gravity forces will be investigated.
The main objectives of this thesis are:

- *To obtain experimental data, numerical solution of equation of motion, and CFD simulation for three different solid spheres in free fall through water*
- *To examine the effect of gravitational hydrodynamic and aerodynamic forces in free fall*
- *To make a comparison among numerical simulation, CFD, and experimental data*
- *To examine Aristotle and Galileo claims regarding the free fall of solid bodies through a quiescent fluid*

1.7 Thesis outline

This thesis is organized as follows. Chapter 2 provides experimental results for free fall of three spherical shaped objects in water. It also provides a discussion of some of the practical aspects of hydrodynamic forces. Chapter 3 discusses the formulation and numerical solution of the equations of motion of solid spheres in a quiescent fluid using the 4th order Runge-Kutta method, and presents results from this approach. Chapter 4 presents CFD simulation of free fall containing a short explanation of theory and the method used in this study. Chapter 5 provides a comparison of the experimental, theoretical, and computational results in this study, summarizes the main conclusions of the study, and presents recommendations for future work.

Chapter 2

Experimental Observation

2.1 On the importance of the experimental approach

Determination of the hydrodynamic/aerodynamic forces acting on a solid particle in a viscous fluid is a fundamental problem in fluid mechanics [9]. This phenomenon has many applications such as multiphase flow, sedimentation and erosion in turbine blades. All of these phenomena involve the same forces as free fall and require prediction of the trajectory of a solid object in a fluid, when the density of the fluid and solid object are different. The ability of a solid particle to behave as a Lagrangian tracer of fluid motion is important, for example, for particle image velocimetry (PIV). This important issue of the prediction of dispersion of solid particles in a fluid has many applications, such as turbomachinery design and piping [13].

Analytical approaches for solving the transient (time dependent) motion of solid object are limited to small Reynolds numbers [14]. However, they can give us insight into the hydrodynamic/aerodynamic forces that are involved. The limitations of analytical methods motivate researchers to either use an analytical approach for simplified forms of the governing equations (such as a quasi steady drag form) or perform experiments to provide a general description of the problem. Generally, we can say that experimental studies in fluid mechanics are important for fundamental research and engineering. However,

experiments are often prohibitively expensive or time-consuming. In some experiments, such as decay of turbulent vortices, there are also practical measurement limitations.

2.2 Free fall experiment

As we discussed previously, experiments play an important role in studying many problems in fluid mechanics. Experimental determination of the free fall of solid bodies through a fluid under gravitational acceleration has a long history in literatures [9] [10]. In this study, we used an apparatus that is used widely at the Concordia University fluid mechanics laboratory. We used spheres with 3 different densities but the same volume, and water as fluid to study three different density ratios (ratio of density of solid to fluid ρ_s/ρ_f).

2.3 Experimental apparatus

Free fall experiments with three different density ratios requires precise measurement of a solid objects position as a function of time.

The experimental apparatus, shown in Figure 2.1, consists of a long transparent cylindrical vessel with an inner diameter $D_C = 0.2$ meters, wall thickness of 0.006 meters and total height of 0.9 meters. The cylinder was filled with tap water, and two black bands were used to denote the test section with a total height $h = 0.195$ meters.

We used three spheres made from different materials: Delerin ($\rho_s/\rho_f = 1.394$), Teflon ($\rho_s/\rho_f = 2.304$), and steel ($\rho_s/\rho_f = 7.894$), where ρ_s and ρ_f are the density of the spherical particle and the fluid, respectively as shown in Figure 2.2. We used spherical shaped solid objects with smooth surfaces to simplify calculation of the drag and added mass force for numerical solution of the equation of motion which will be discussed in Chapter 3.

Figure 2.1: Free fall apparatus

A high speed camera shown in Figure 2.3 was used to record the trajectory of the spheres. This camera is a Basler acA640-750um delivering videos at 751 frames per second with VGA resolution (more specification can be found in Appendix B). It captures a sequential series of images that are recorded at high frame rates and played back in slow-motion to

allow us to capture, measure, and understand the position of spheres as a function of time.

Figure 2.2: The Delerin, Teflon, and steel spheres

Figure 2.3: The High speed camera used to record the trajectory of the spheres

2.4 Experimental setup

As discussed earlier, in this study we are investigating the trajectory of falling spheres in quiescent water. Since the camera is fixed at a stationary point, and its distance to the apparatus can not increase from a special value (0.5 meters) due to intransparency of the pictures, we can not take a large height to examine the displacement of the spheres.

The density of tap water is assumed to be 998.1 (kg/cubic meters), whereas its viscosity is 10^{-3} Pascal at $T = 20$ °C [15]. To avoid air entertainment, the particles were initially submerged and held in a place under the water surface by a mechanical support and then released. The particle trajectory was recorded by the high-speed camera at 750 frames per second. The recorded sequences of the particle motion were analyzed using the MATLAB [16] image processing toolbox.

In order to eliminate random perturbations, we repeated the experiment three times and then took an ensemble average to obtain a displacement curve. Finally, we extracted the corresponding velocity curve to the average displacement by using a centered finite difference method as:

$$\overline{V} = \frac{\overline{x_{i+1}} - \overline{x_{i-1}}}{2\Delta t}, \tag{1}$$

where $\overline{V}$ is ensemble average velocity and $\overline{x}$ In order to ensure that the velocity curve is independent of size of Δt, we obtained the average velocity curve from average displacemeny using different time steps and observed small difference between the curves. Figure 2.4 shows two different velocity curves.

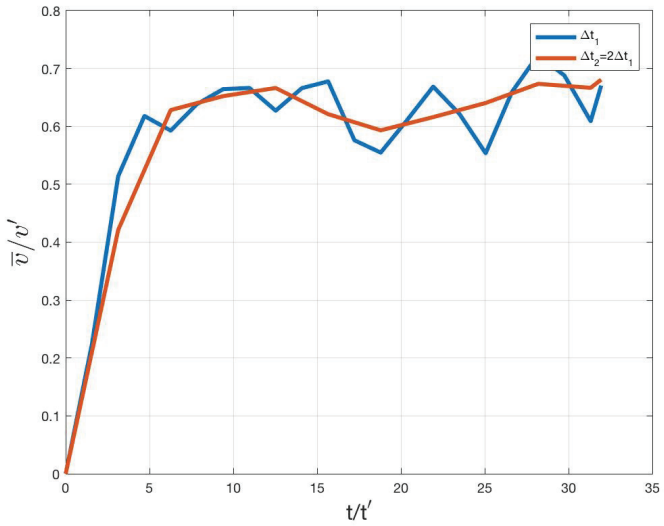

Figure 2.4: Difference between 2 velocity curves derived with different time steps

2.5 Dimensionless quantities

In order to make general conclusions about the free fall of spheres through a quiescent fluid we chose to non-dimensionalize our results (dimensional analysis). In dimensional analysis, dimensionless quantities are pure numbers and, as such, always have dimension of unity. Therefore, these quantities can be generalized to any geometry or configuration with having same dimensionless quantities.

In this dissertation, we used the diameter of the sphere as characteristic length, the required time for the spheres to move equal to their diameters under the gravitational acceleration in vacuum situation as the characteristic time, and the velocity at this time as

the characteristic velocity. Finally, density ratio completes set of dimensionless quantities. These quantities are defined mathematically as

$$t' = \sqrt{\frac{D}{0.5g}}, \tag{2}$$

as the characteristic time, and:

$$v' = gt', \tag{3}$$

as the characteristic velocity.

As noted, D (diameter of the sphere) as the characteristic length, ρ_s/ρ_f as density ratio, and gravitational force ($F' = mg$) as the characteristic force.

Reynolds number is defined for the particle as

$$Re_p = \frac{VD}{\nu} \tag{4}$$

where ν is the kinematic viscosity of water.

The dimensionless quantities built using these characteristic quantities are independent of the apparatus, and can be used for any free fall of spheres having the same dimensionless parameters.

2.6 Uncertainity in experimental results

As discussed previously, experiments have limitations and uncertainities. For example, as we measured the diameter of the spheres with a micrometer with an accuracy of 0.00005 meters, we observed that real diameter of spheres are 0.005 ± 0.0001 meters. We observed the same thing with mass of the spheres ($m \pm 0.001$ g). We also know that the support which is used to release the spheres in fluid makes some random perturbations in the fluid at the moment of release.

In fact, these uncertainities cause error. Error is defined as the difference between the true value of a measurement and the recorded value of a measurement. Errors are divided

to two major categories, random and bias or systematic errors. Random error has no preferred direction, so we expect that averaging over a large number of observations will yield a net effect tending to zero. On the other hand, bias has a net direction and magnitude so that averaging over a large number of observations does not eliminate its effect. So, it is usually difficult to address. Random error corresponds to imprecision, and bias to inaccuracy. In our study, we repeated the experiment to reduce random errors, such as release perturbation and we tried to use as accurate as possible equipments to avoid bias errors.

2.7 Experimental Results

2.7.1 Impact quantities

It has been proven experimentally that the free fall of any particle in a quiescent fluid has two parts. A transient part from the moment the particle is released until its velocity becomes approximately steady (terminal velocity). Then a quasi-steady state period after the object reaches this terminal velocity.

Table 2.1 demonstrates the impact time and velocity as well as terminal Reynolds number from the current experimental study. Impact Reynolds number is calculated with the velocity of solids spheres when they reach a dimensionless displacement of 39 ($\frac{x}{D} = 39$) as

$$Re_{p_i} = \frac{V_i D}{\nu}. \tag{5}$$

Sphere Material	$\frac{\rho_s}{\rho_f}$	h/D height studied	V_i/V' impact velocity	t_i/t' Bed impact time	Re_{p_i}
Delrin	1.394	39	0.689	32.02	1075
Teflon	2.304	39	1.31	17.74	2045
Steel	7.794	39	3.36	8.55	5245

Table 2.1: Results from free fall of three density ratios based on experiments

2.7.2 Experimental curves

Figures 2.5a, 2.5c, and 2.5e show the displacement curves for three individual experiment and the ensemble average curve for each density ratios ($\rho_s/\rho_f = 1.394$, $\rho_s/\rho_f = 2.304$, and $\rho_s/\rho_f = 7.794$). Figures 2.5b, 2.5d, and 2.5f show the velocity graphs corresponding to average displacement curves. As can be seen in the figures, the velocity is observed to fluctuate when approaching the terminal velocity. These fluctuations are possibly associated with a temporal evolution of the solid body wake (turbulent vortices around solid body). It is observed that the velocity is no longer a monotonical function of time, it fluctuates between periods of increased and decreased velocity. For this to happen, the acceleration of the particle must change its sign, in particular the reaction of the wake on the particle is sufficient to overcome the gravitational force. Note that the particle Reynolds number is close to 1075, 2045, and 5245 for $\rho_s/\rho_f = 1.394$, $\rho_s/\rho_f = 2.304$, and $\rho_s/\rho_f = 7.794$ (Delerin, Teflon, and steel) respectively.

Figures 2.6, and 2.7, as well as Table 2.1 show the displacement and velocity curve for different density ratios respectively. As density ratio increases the sphere moves the dimensionless length of 39 in the shortest time, and it reaches a higher terminal velocity. We also observe that by increasing the density ratio the displacement and velocity curves approach those of free fall in a vacuum. It is clear that as density ratio increases $F_g - F_b$ is larger.

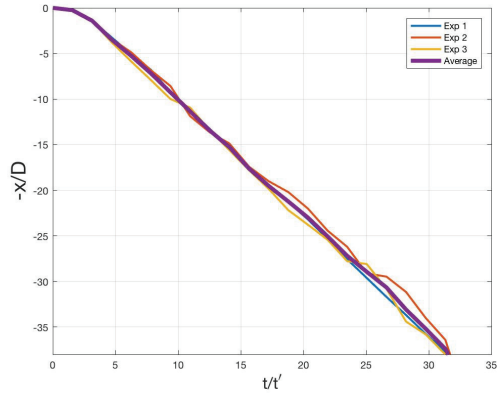

(a) Dimensionless displacement curves for three individual experiments and their average for $\rho_s/\rho_f = 1.394$ (Delerin)

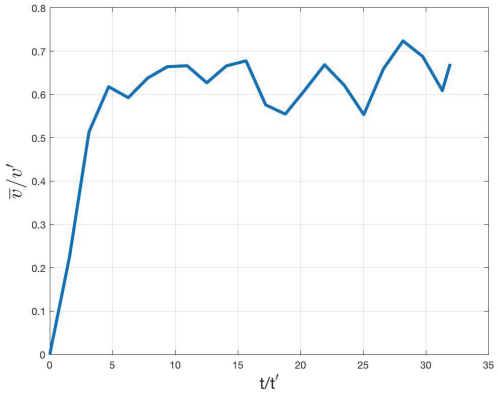

(b) Dimensionless velocity curve corresponding to average displacement for $\rho_s/\rho_f = 1.394$ (Delerin)

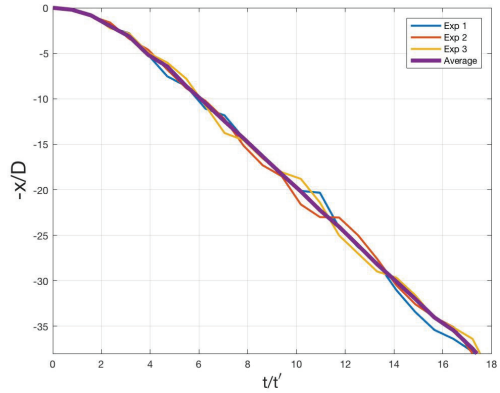

(c) Dimensionless displacement curves for three individual experiment and average for $\rho_s/\rho_f = 2.304$ (Teflon)

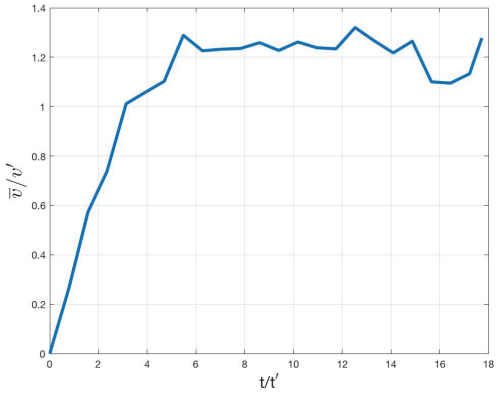

(d) Dimensionless velocity curve corresponding to their average displacement for $\rho_s/\rho_f = 2.304$ (Teflon)

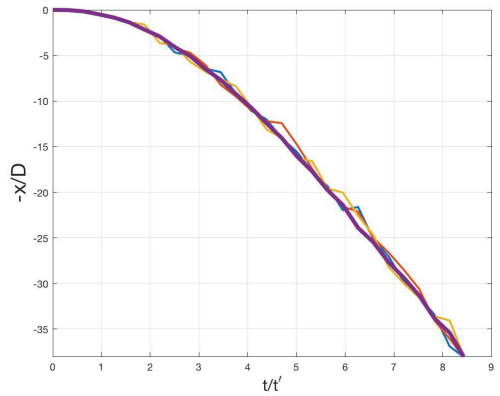

(e) Dimensionless displacement curves for three individual experiment and their average for $\rho_s/\rho_f = 7.794$ (steel)

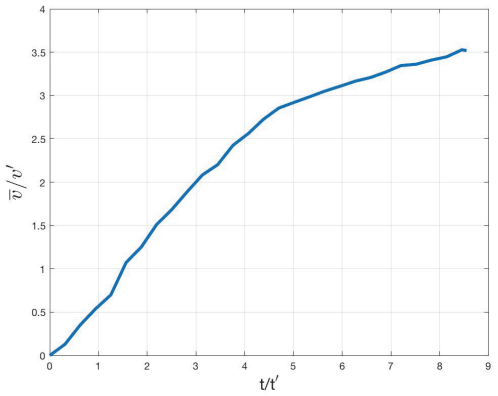

(f) Dimensionless velocity curve corresponding to average displacement for $\rho_s/\rho_f = 7.794$ (steel)

Figure 2.5: Experimental curves

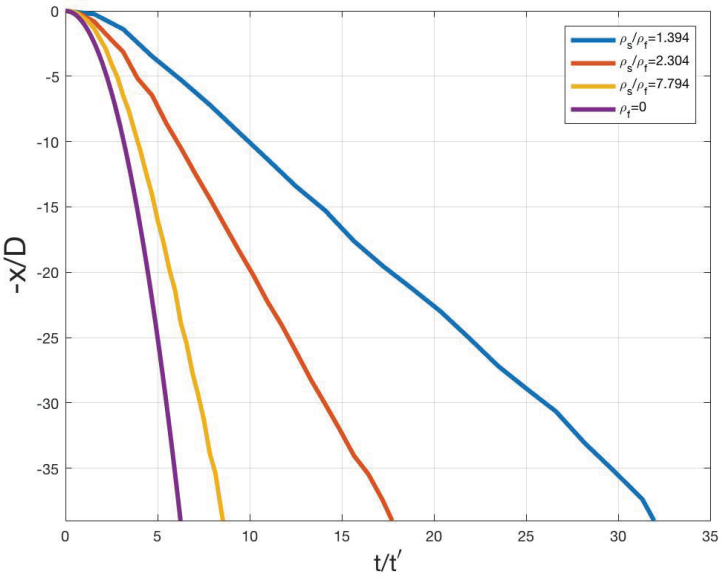

Figure 2.6: Dimensionless displacement curves

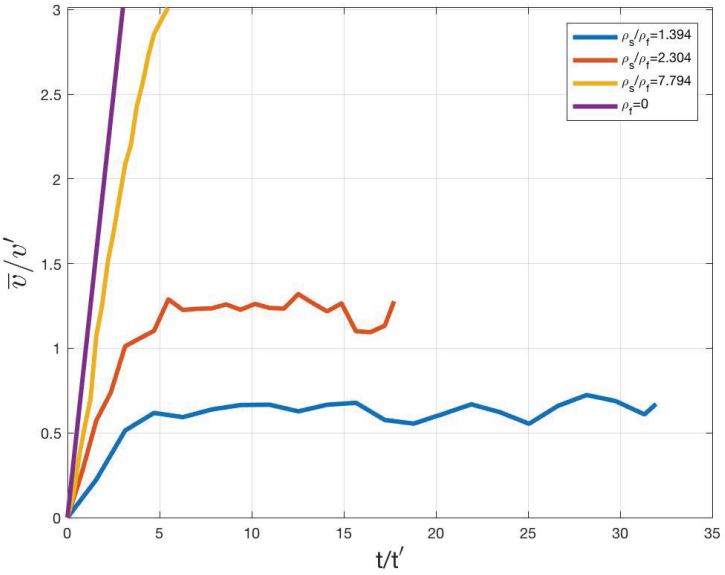

Figure 2.7: Dimensionless velocity curves

Chapter 3

Mathematical Formulation and Numerical Solution

3.1 Basset-Boussinesq-Oseen equation

In dynamics, Newton's second law is used to describe the motion of a rigid body. In free fall of a rigid body, based on Newton's second law solid body falls under the gravitational force. In addition to the gravitational force, there are other major forces such as buoyancy, drag and added (virtual) mass [17]. There are also other minor forces such as the Basset (history) force and the pressure gradient. All of these forces are deduced from the Navier-stokes equations and will be defined and discussed individually in this chapter.

The describing equation of motion for free fall was first introduced by Stokes [18], and later Basset, Boussinesq, and Oseen independently, which contains all of the above forces. They examined the effect of a transient drag force on a solid object passing through a fluid. In physics, the equation of motion of free fall or rise of a solid object through a fluid named after these three scientist as BBO equation. This equation can be written as [17]

$$\frac{\pi}{6}\rho_s D^3\frac{dV_s}{dt} = 3\pi\mu D(V_f - V_s) - \frac{\pi}{6}D^3\nabla p + \frac{\pi}{12}\rho_f D^3\frac{d}{dt}(V_f - V_s) + \frac{3}{2}D^2\sqrt{\pi\rho_f\mu}\int_0^t \frac{1}{\sqrt{t-\tau}}\frac{d}{d\tau}(V_f - V_s)d\tau + \frac{\pi}{6}\rho_s D^3 g + \frac{\pi}{6}\rho_f D^3 g + \sum_k F_k, \tag{6}$$

where: ρ_s is solid sphere density, ρ_f is fluid density, D is solid sphere diameter, V_f is fluid velocity, V_s is particle velocity, μ is fluid dynamic viscosity, p is fluid pressure, τ is kernel time, g is gravitational acceleration, t is time, and F_k are other forces.
The terms on the right-hand side are, respectively, the:

- Drag force (Stoke's drag)
- Pressure gradient
- Added or virtual mass
- Basset or history force
- Gravity force
- Buoyancy force
- Other forces

Before, going through the numerical solution of this equation it is useful to know more about the physical interpretation of these forces.

3.1.1 Drag force

The drag force causes a particle tends to follow the motion of the fluid Drag force consists of viscous drag as well as pressure drag at the surface of the sphere. The drag force is typically one of the most dominant terms in BBO equation. For highly viscous flow (low particle Reynolds number) an analytical solution can be obtained for the drag force (Stokes 1851) [18]:

$$F_D = 3\pi\mu D(V_f - V_s). \tag{7}$$

At higher particle Reynolds numbers, on the other hand, empirical correlations are needed and are expressed via a drag coefficient:

$$C_D = \frac{F_D}{\frac{1}{2}\rho_f (V_f - V_s)^2 A_s}. \tag{8}$$

However, based on experimental data (Schiller and Naumann, 1933) [19] a relation for the drag coefficient can be drawn as:

$$C_D = \frac{24}{Re_p}(1 + 0.15 {Re_p}^{0.687}). \tag{9}$$

In Equation (9) once the flow (particle velocity), reaches to critical velocity (critical Re_p) the C_D tends to 0.44.

There are additional considerations in determining the drag coefficient:

- Turbulence of the surrounding fluid reduces the critical Reynolds number to about 1000 [20].
- Surface roughness also causes a reduction in the critical Reynolds number [20].
- With increasing particle concentration the drag is considerably increased (hydrodynamic interaction)

In this study, since we are dealing with a range of Reynolds number from zero to 5000, we decided to use Equation 9 as the drag coefficient to find the drag force.

3.1.2 Pressure gradient force

The pressure gradient force acting on the particle is due to local pressure gradient and shear stresses in the flow [21]. Pressure gradient can be derived from Navier-Stokes equations:

$$F_p = \frac{m_s}{\rho_s}(-\nabla p + \nabla \tau). \tag{10}$$

With the Navier-Stokes equations we find that

$$-\nabla p + \nabla \tau = \rho_f \left(\frac{DV_f}{Dt} - g \right). \tag{11}$$

This yields the total pressure force as

$$F_p = m_s \frac{\rho_f}{\rho_s} \left(\frac{DV_f}{Dt} - g \right), \tag{12}$$

where the right hand side shows the buoyancy and pressure gradient force.

3.1.3 Added mass

As a solid object moves through a fluid, some fluid particles around solid object move along with it. In other words, when the body accelerates, a number of fluid particles must also accelerate alongside with the solid particle. Thus, higher amount of force is required to accelerate a body in a fluid than in vacuum. Since force equals mass times acceleration, we can consider the additional force in terms of an imaginary mass (added mass). We can derive the added mass of an object by considering the hydrodynamic/aerodynamic forces acting on it as it accelerates [22]. Consider a sphere of radius, R or diameter D, accelerating at rate of

$$\frac{\partial V}{\partial t} = \dot{V}. \tag{13}$$

If we assume that the sphere is idealized to move in x direction then we can find the added mass force in the x-direction by integrating the pressure over the area projected in the x-direction:

$$F_x = \int p dA_x, \tag{14}$$

where:

$dA_x = sin\theta dA$, $dA = 2\pi r ds$, $r = Rsin\theta$ and $ds = Rd\theta$

where

A_x is x-direction projection of the surface area,

A is the surface area,

and ϕ is the flow rate

Also via the unsteady Bernoulli equation we can say

$$p = -\rho[\frac{\partial \phi}{\partial t} + \frac{1}{2}|\nabla \phi|^2], \tag{15}$$

and we know that for axisymmetric flow around a sphere

$$\phi = Vcos\theta \frac{R^3}{2r^2}, \tag{16}$$

and

$$\frac{\partial \phi}{\partial t}\Big|_{r=R} = \dot{V}cos\theta \frac{R}{2}, \tag{17}$$

Similarly

$$\frac{1}{2}|\nabla \phi|^2\Big|_{r=R} = \frac{1}{2}\left|\left(Vcos\theta \frac{R^3}{r^3}, -Vsin\theta \frac{R^3}{2r^3}\right)\right|^2 = \frac{1}{2}\left[V^2cos^2\theta + \frac{1}{4}V^2sin^2\theta\right], \tag{18}$$

Therefore

$$\begin{aligned} F_y &= \int_0^\pi \left[-\rho\left[\frac{\partial \phi}{\partial t} + \frac{1}{2}|\nabla \phi|^2\right]\right] cos\theta 2\pi R^2 sin\theta d\theta \\ &= \int_0^\pi \left[-\rho\left[\dot{V}cos\theta \frac{R}{2} + \frac{1}{2}(V^2cos^2\theta + \frac{1}{4}V^2sin^2\theta)\right]\right] cos\theta 2\pi R^2 sin\theta d\theta \\ &= -\rho 2\pi R^2 \dot{V}\frac{R}{2}\int_0^\pi sin\theta cos^2\theta d\theta - \rho 2\pi R^2 \frac{1}{2}V^2 \int_0^\pi \left[sin\theta cos^2\theta + \frac{1}{4}sin^3\theta cos\theta\right] d\theta \\ &= -\frac{2}{3}\rho\pi R^3 \dot{V}, \end{aligned} \tag{19}$$

where $\dot{V}$ is the acceleration of the body, and the negative sign indicates that the force is in the negative x direction, opposing the acceleration. Thus, the equation must accommodate

this extra force, and we can say the added mass is:

$$m_a = -\frac{2}{3}\rho\pi R^3. \tag{20}$$

3.1.4 Basset force (history force)

As was discussed in the drag force section, the drag force only depends on the value of the Reynolds number. Consequently, we can say that it is assumed that the boundary layer is fully developed. However, as we know development of the boundary layer is a time dependent process and it cannot form instantaneously. As a result, it can be said that the drag term in the BBO equation is not an appropriate representation of the real physical drag force for an accelerating particle. The Basset force accounts for this lagging of the unsteady boundary layer development, as well as the solid particle wake [23]. To capture these unsteady effects, an integral over time is required from the start of particle motion up to the current time. A kernel which is a function of (t, τ) connects the acceleration of the particle at time t to the resulting force at time τ. (Mei et al., 1991 [24]; Loth and Dorgan, 2009 [25]; Mordant and Pinton, 2000 [26]).

3.1.5 Simplified BBO equation

In this thesis, we decided to neglect the pressure gradient, since this force is only important if large fluid pressure gradients exist and if the particle density is smaller than or similar to the fluid density [12]. Therefore, with respect to the quiescent fluid assumption, the BBO equation is simplified to

$$\begin{aligned}\frac{\pi}{6}\rho_s D^3\frac{dV_s}{dt} = &-\frac{1}{2}\rho_f C_D A {V_s}^2 + \frac{\pi}{12}\rho_f D^3\frac{d}{dt}(-V_s) + \frac{\pi}{6}\rho_s D^3 g \\ &- \frac{\pi}{6}\rho_f D^3 g + \frac{3}{2}D^2\sqrt{\pi\rho_f\mu}\int_0^t \frac{1}{\sqrt{t-\tau}}\frac{d}{d\tau}(-V_s)d\tau,\end{aligned} \tag{21}$$

where

$$C_D = \frac{24}{Re}(1 + 0.15{Re_p}^{0.687}), \tag{22}$$

and based on [27] the time kernel is defined as:

$$\tau = \frac{1}{\sqrt{t}}. \tag{23}$$

3.2 Numerical solution

We used MATLAB and the 4th order Runge-Kutta method to solve the simplified BBO equation numerically (See Appendix A). We obtained displacement and velocity profiles for the three density ratios $\rho_s/\rho_f = 1.394$, $\rho_s/\rho_f = 2.304$, and $\rho_s/\rho_f = 7.794$ and a fixed dimensionless height of $\frac{x}{D} = 39$.

3.2.1 Impact quantities

Table 3.1 shows dimensionless time, velocity and Reynolds number after dimensionless displacement of 39 ($\frac{x}{D} = 39$).

Sphere Material	$\frac{\rho_s}{\rho_f}$	h/D height studied	V_i/V' impact velocity	t_i/t' Bed impact time	Re_{p_i}
Delrin	1.394	39	0.709	31.07	1100
Teflon	2.304	39	1.37	17.02	2140
Steel	7.794	39	3.39	8.24	5295

Table 3.1: Results from free fall of three density ratios based on numerical solution

3.2.2 Numerical solution curves

Figures 3.1, 3.2 as well as Table 3.1 show displacement and velocity graphs for each density ratios based on numerical solution of the equation of motion. It can be seen that terminal velocity increases as the density ratio increases. It is also clear that since the equation

of motion does not consider turbulent chaotic effects, no oscillation can be observed in the graphs. In Figure 3.3, we can see that the net force is very large at the beginning of the motion. However, it decreases as the velocity of spheres increases, and tends to approximately zero at the end, once the spheres reach their terminal velocity (steady state condition).

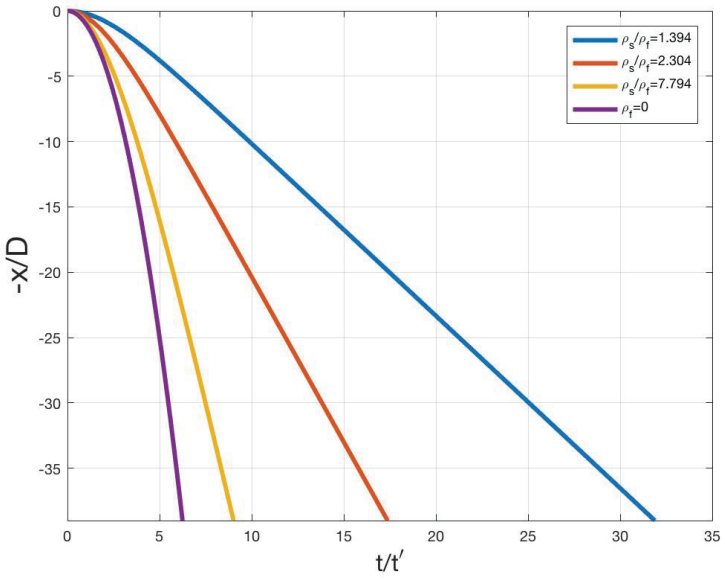

Figure 3.1: Dimensionless displacement curves

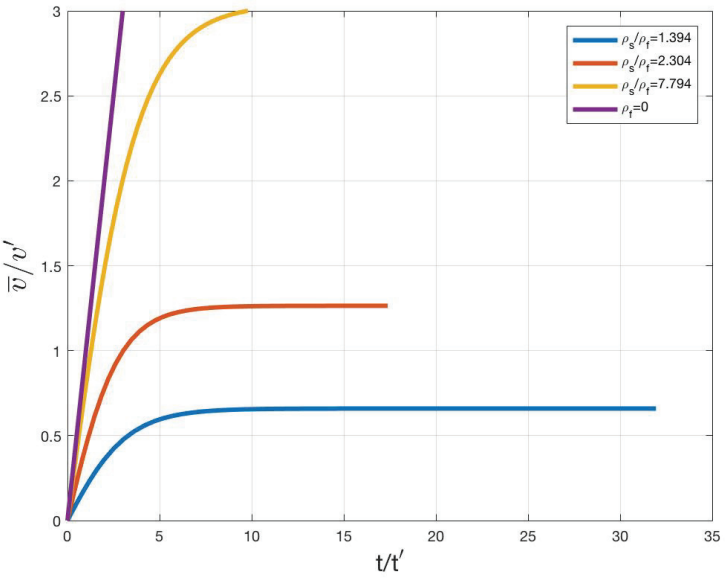

Figure 3.2: Dimensionless velocity curves

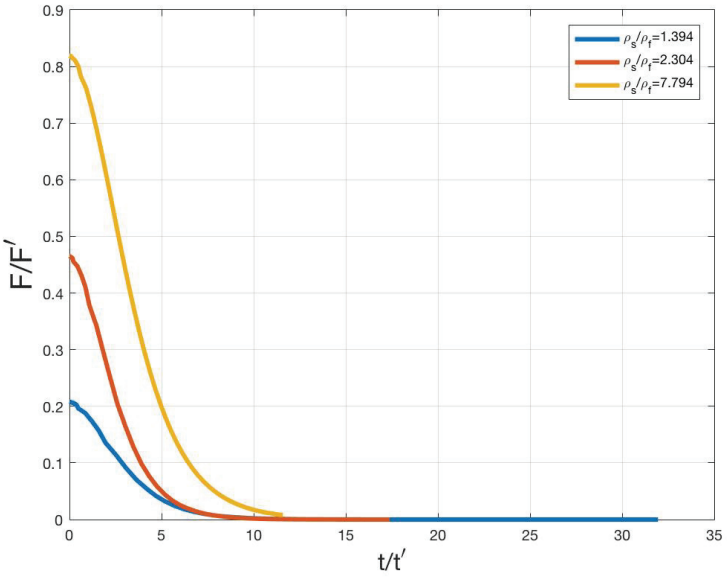

Figure 3.3: Dimensionless Force curves

3.3 Contribution of each transient force

In Figures 3.4a, 3.4b, and 3.4c, we studied the contribution of each force (each term in BBO equation), to the total force of falling spheres. Since the magnitude of the Basset force is relatively small with respect to other forces, these figures are shown in logarithmic scale. It is clear that the value of gravitational and buoyancy forces and their subtraction $F_g - F_b$ is constant in time and increases as the density ratio increases. It can be seen in these figures that the total force is equal to the summation of all forces. Furthermore, the Basset and added mass forces are transient terms which tend to zero once the motion of the sphere becomes steady. It is clear that Basset force is small accounting for less than 1 percent effect on the total force. However, the added mass has larger contribution to the total force, particularly in the accelerating phase of the motion. As expected the drag force also increases as the velocity of the sphere increases. Moreover, we can see that value of added mass force remains constant until the drag force reaches the same value. This equal value happens at the same dimensionless time ($t/t' \approx 0.88$) for all density ratios.

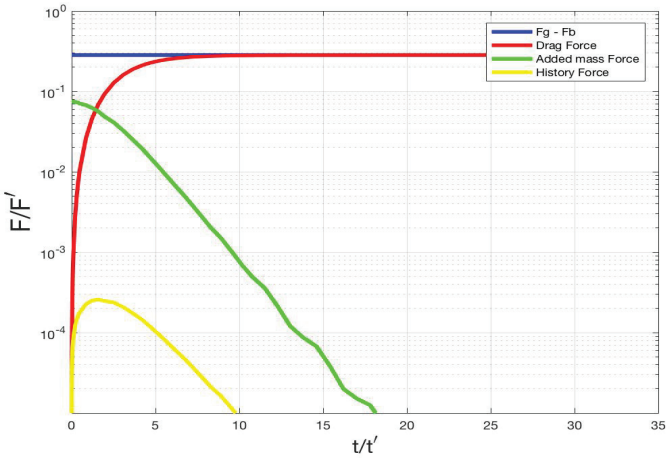

(a) Delerin sphere

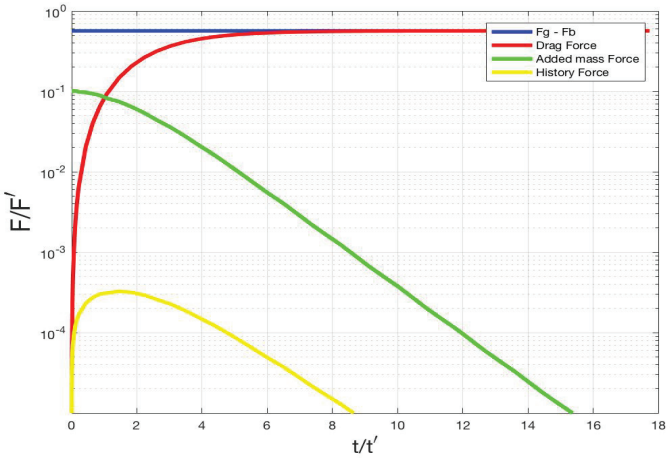

(b) Teflon sphere

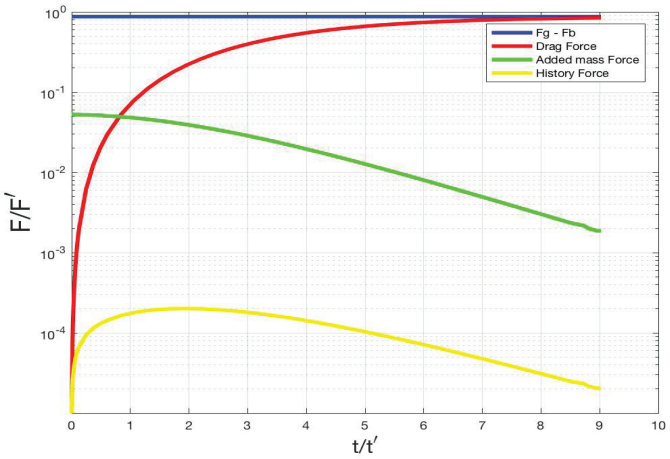

(c) Steel sphere

Figure 3.4: Contribution of each force on the spheres

Chapter 4

CFD Simulation

4.1 Theory

4.1.1 Finite volume analysis and finite volume method

Many of the laws in physics are space and time dependent. They are often expressed in terms of partial differential equations (PDEs) such as fluid flow, thermal transport, wave propagation, etc. Most applications involve complex geometries, such that these PDEs cannot be solved using analytical approaches. Instead, a numerical approximation of the equations can be made, typically based on different types of discretizations. As was discussed in the introduction, these discretization methods approximate the continuous PDEs with discrete forms, which can be solved using numerical methods. The solutions to the numerical model equations are an approximation of the real solution to the PDEs. The finite volume method (FVM) is such a numerical method used to compute approximate solutions to PDEs.

The FVM has been used successfully in the modeling of several aerospace and mechanical engineering problems [28]. Application of the FVM covers a variety branches of physics and engineering. One of the most exciting aspects of its application is to couple

problems like fluid-structure interaction, thermo-mechanical, thermo-chemical, thermo-chemo-mechanical, and bio-mechanical engineering. Some alternative methods have been proposed in recent years to be used instead of the finite volume method. However, the finite volume method remains popular due to its simplicity, ease of implementation, and suitability for complex geometries.

4.1.2 How the FVM works

The general methodology of the finite volume method consists of:

- Decomposition of the domain into elements considered as control volumes (mesh generation).
- Deriving integral formulations for these control volumes.
- Approximation of integrals using numerical integration and algebraic operations.
- Approximation of the values and differentials using interpolation
- Assembling the solution

The first step, is to generate a suitable mesh. In the finite volume method, depending on the solver we can use different type of elements such as tetrahedral, hexahedral, pyramid and triangular prisms. However, the finite volume codes are usually more efficient with hexahedral shaped elements [29].
The second step involves forming integral relations for each control volume in the mesh. For example, for a general transport equation of the form:

$$\frac{\partial}{\partial x_i}\left(\rho v_i \phi - \alpha \frac{\partial \phi}{\partial x_i}\right), \tag{24}$$

where ϕ is the transport value, x_i are spatial directions, ρ, and α are constants, we can form the integrals as:

$$\iint_{\Gamma}\left(\rho v_i \phi - \alpha \frac{\partial \phi}{\partial x_i}\right) n_i d\Gamma = \iiint_{\Omega} f d\Omega, \tag{25}$$

where Γ is is the surface of the element, Ω is the volume of the element, and n_i are normals of the surface. In the third step, we approximate these integrals to:

$$\sum_c \dot{m}_c \phi_c - \sum_c \alpha n_i \delta\Gamma (\frac{\partial \phi}{\partial x_i})_c = f \delta\Omega, \tag{26}$$

where $\dot{m}_c$ is mass flow rate. In step four and five we typically interpolate between the values of function in control volumes to find the values on the surfaces of each element (control volumes).

4.1.3 Recent developments and history of finite volume methods

The finite volume method could be said to have its origins in the work of Euler as early as the 16th century. However, the earliest mathematical formulations on FVM can be found in the works of Schellback (1851) and Courant (1943) [30] [31]. Later, the finite volume method was independently developed by engineers to address structural mechanics problems related to aerospace and mechanical engineering.

In recent decades, finite volume methods have been developed in two general categories [32]. The first category is considered as an extension of finite difference schemes for complicated geometries and irregular meshes. Methods in this category usually reconstruct a polynomial to satisfy the main principle and maintain flux consistency between elements. Higher order methods in finite volume methods are considered as a relatively new method is in this category. High order formulations take into consideration a high-order polynomial reconstruction in their calculations. Good examples of methods in this Category are WENO (Weighted Essentially Non-Oscillatory) and ENO (Essentially Non-Oscillatory) finite volume schemes [32]. Second category is considered as a development in the Galerkin form by taking advantage of two different meshes, including one primary mesh to approximate exact solution, and a dual mesh to discretize the equation [32]. A good example of methods in this category is DG (Discontinuous Galerkin methods) [32].

Recent developments of finite volume methods are considered to have two main advantages. First, higher order of accuracy, that only depends on the order of polynomials used for reconstruction. Second, higher compatibility with complicated geometries [32]. However, higher-order methods are often less robust than conventional second-order schemes. Furthermore, the lack of commercially available high-order solvers has motivated the use of a second-order accurate solver in this study.

4.1.4 Fluid-structure interaction "FSI"

4.1.4.1 Introduction

In the case of free fall, in addition to a normal fluid flow domain which is solved with the finite volume method we have a solid domain with its own dynamics. This has a high level of complexity, since we have a solid domain moving through a fluid domain under the effect of body forces, such as gravity, buoyancy and the interaction of forces between the fluid particle and its boundary. Such complexity requires a fluid-structure interaction approach, which is discussed in this section. Underlying Bazilevs et al. [33] the interactions between fluid particles and immersed solid structures are also nonlinear phenomena that have applications in a wide range of scientific and engineering disciplines. In fluid-structure interaction (FSI) problems, one or more solid structures interact with an internal or surrounding fluid flow. FSI methods play important roles in many engineering fields. However, so far a comprehensive approach for these problems is still a challenge due to their strong nonlinearity and multidisciplinary nature.

4.1.4.2 FSI definition and formulation

In order to define the fluid structure problem, a mathematical formulation is necessary. Based on Hou et al. [34] whole domain, which is denoted by Ω, has a boundary Γ. The domain includes the solid object, $\overline{\Omega_s}$, and the fluid domain which is water in our case, $\overline{\Omega_f}$

; i.e., $\Omega = \overline{\Omega_s} \cup \overline{\Omega_f}$. The fluid-structure interface is defined by $\Gamma_s = \overline{\Omega_s} \cap \overline{\Omega_f}$. The equations of motion for the fluid and structure are expressed in the same index form [34].

$$\rho \dot{v_i} - \sigma_{ij,j} + f_i = 0, \tag{27}$$

where f_i is the body force, such as gravity and buoyancy in our case. Specifically, in the solid domain, the equation is written as [34]:

$$\rho^s \dot{v_i}^s - \sigma^s_{ij,j} + f^s_i = 0 \qquad in \quad \overline{\Omega_s}, \tag{28}$$

where the superscript, s, shows the solid domain quantities, and the velocity, v^s_i , is the material (or total) time derivative of the displacement field. As given, this equation is a Lagrangian description. The first two terms in this equation are representing inertia and internal stresses, respectively. If we consider linear elastic materials, the structural stress follows the linear Hooke's law:

$$\sigma^2_{ij} = \lambda \delta_{ij} \epsilon_{ll} + 2G\epsilon_{ij}, \tag{29}$$

where the structural stress σ^s_{ij} is a function of the strains, ϵ_{ij}, and the Lame constants λ and G, which are defined by:

$$\epsilon_{ij} = \frac{1}{2}(u_{ij} + u_{ji}), \tag{30}$$

$$G = \frac{E}{2(1+\nu)}, \tag{31}$$

$$\lambda = \frac{E\nu}{(1+\nu)(1-2\nu)}, \tag{32}$$

where E and ν are the Young's modulus and the Poisson's ratio, respectively. however, in our case, for simplicity we decided to consider the solid domain as a rigid body. Consequently, the second term in the (29) is equal to zero.

The fluid domain, is described by [34]:

$$\rho^f \dot{v_i}^f - \sigma^f_{ij,j} + f^f_i = 0 \qquad in \quad \overline{\Omega_f}, \tag{33}$$

As can be seen, this equation provides an Eulerian description. In a similar way to the solid domain, in the inertia term, there is:

$$\dot{v_i}^f = \frac{dv_i{}^f}{dt} = \frac{\partial v_i{}^f}{\partial t} + v_j{}^f + v_{ij}{}^f. \tag{34}$$

In the free fall of solid spheres case in water, we assume that we are dealing with an incompressible Newtonian fluid, so the fluid stress σ^f_{ij} can be described by

$$\sigma^f_{ij} = -p\delta_{ij} + \tau_{ij}, \tag{35}$$

where

$$\tau_{ij} = 2\mu(e_{ij} - \frac{\delta_{ij}e_{kk}}{3}), \tag{36}$$

and

$$e_{ij} = v^f_{ji} + v^f_{ij}. \tag{37}$$

In this equation the static pressure p, is the necessary force to enforce the incompressibility condition $v^f_{ij} = 0$.

In order to maintain the no-slip condition along the fluid and solid interface Γ_s, the following Dirichlet and Neumann conditions are considered:

$$v_i{}^s = v_i{}^f \qquad on \quad \Gamma_s, \tag{38}$$

which describes the equality of velocities at the interface, and

$$\sigma_{ij}{}^s n_i = \sigma_{ij}{}^f n_i \qquad on \quad \Gamma_s, \tag{39}$$

which is the differentiation of the displacement (deformability) condition that both fields sharing the same interface, in other words

$$x_i{}^s = x_i{}^f \qquad on \quad \Gamma_s. \tag{40}$$

Fluid-structure interaction methods is divided to two major categories:

- Conforming mesh methods
- Non-conforming mesh methods

These categories arose from the procedure of transmission conditions [35]. In other words, conforming mesh methods track the motion of the solid object and its interface with the fluid to enforce the no-slip condition. For the conforming mesh methods dynamic mesh generation and a mesh update are used at every time step. However, the non-conforming mesh methods focus on the enforcement of the Dirichlet boundary condition. In fact, the non-conforming mesh method is derived from the Lagrangian multipliers theorem [34]. Lagrangian multipliers act as source term in the fluid domain equations to represents solid boundaries in the fluid. Accuracy in determining the Lagrangian multipliers affects the accuracy of the numerical solution [36].

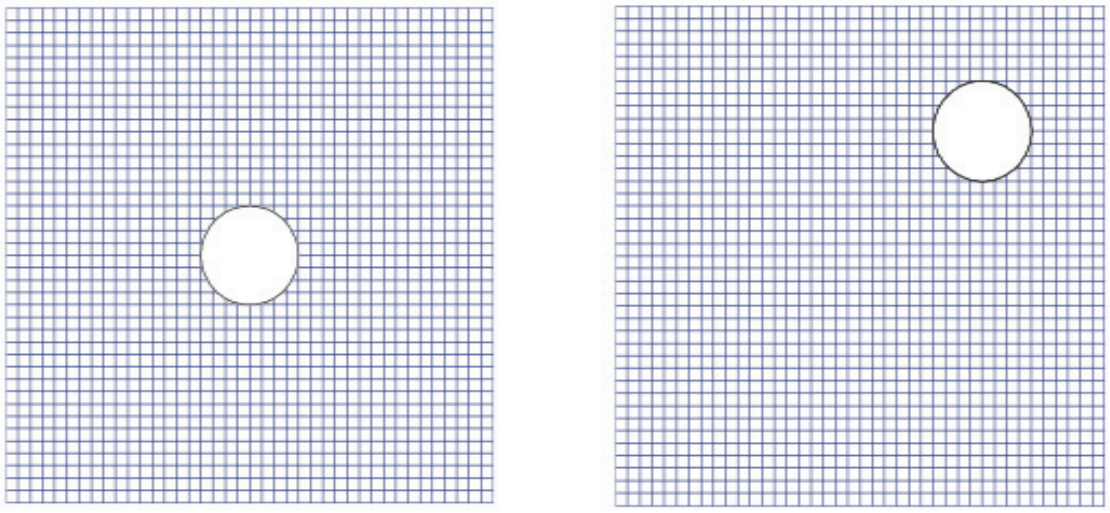

Figure 4.1: Non-conforming mesh at 2 different time steps

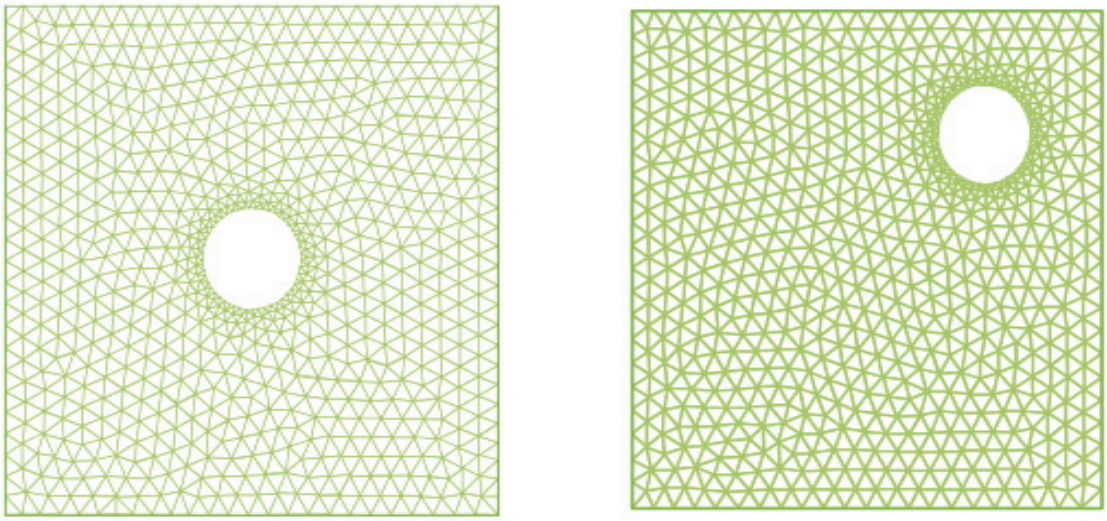

Figure 4.2: Conforming mesh at 2 different time steps

4.1.4.2.1 Conforming mesh methods

Conforming mesh methods usually have to update the mesh at each time step, so we can say that in these methods there are three fields, describing the fluid domain, solid body dynamics, and mesh movement. In this method, we solve the fluid domain in a time step with an assumed solid boundary location. Then, the resulting pressure and stress are applied to the solid object as external forces in addition to the buoyancy and gravity (body forces). Then the computation based on solid dynamics is conducted and at the end, based on these computed position of the solid object the mesh will be updated. Once a new mesh is created, new interface locations will be revealed that will be used at the next time step. One of the most popular fluid-structure interaction with conforming mesh methods is the Arbitrary Lagrangian Eulerian method (ALE) [34]. In this method, the moving mesh is explicitly related to the fluid domain equations. In this model we have a special kind of material derivative which is expressed as [33]

$$\frac{dv_f}{dt} = \frac{\partial v_f}{\partial t} + (v_f - U).\nabla v_f, \tag{41}$$

where U is the velocity of the fluid mesh.

4.1.4.2.2 Immersed methods (non-conforming mesh method)

Many notable non-conforming fluid-structure solvers are based on the immersed methods [33]. In this method, we have two sets of governing equation for both the solid and fluid domains, which are solved individually. However, in each equation there is cross-term representing the effects of the other domain. In order to avoid mesh updates, we add force equivalent terms to the fluid equations to represent interactions. The solid object in this method (immersed solid) can be a 2 dimensional curve or a 3 dimensional rigid or flexible body [34].

The immersed methods (non-conforming mesh methods) work by using Lagrangian multipliers. Meanwhile, the immersed method itself is categorized to two types of [37]

- Immersed boundary method
- Immersed domain method

Peskin(1977) [36] first introduced the immersed boundary method for studying blood flow through a beating heart. Since then, this method has been widely used in different branches of fluid mechanics. In this method, the fluid equations are solved with an additional term representing the immersed boundary. Once the fluid velocity has been determined we are able to determine the fluid-structure interaction force by using the no-slip condition on the interface and then we can compute the forces and moments on the solid body and determine its displacement and velocity. Actually, we can say in the immersed boundary method we must solve the whole fluid domain with an Eulerian mesh configuration with the FSI term at each time step to determine the position and velocity of the solid domain. We can say that in immersed boundary methods we assume that our solid domain does not have a volume, instead, we try to consider its presence by fluid structures interaction terms.

The immersed boundary method is much simpler in comparison to the conforming mesh methods. In principle, the immersed boundary method deals with structures that do not occupy volumes, e.g., a fiber or a closed curve in 2D space and a membrane in 3D

space [12]. However, it has its own disadvantages. For example, the solid object instantaneous response to the fluid particles motion may not be accurately modeled [38]. In order to have a better model of these responses, the immersed domain method has been introduced. In the immersed domain method it is assumed that an artificial fluid has covered the solid domain. So the whole domain consists of real fluid and artificial fluid and no-slip condition is implied on the interface of the artificial and real fluid and matches the position and velocity between the real fluid and solid structure (artificial fluid). To enforce this no-slip condition a fluid structure force is applied on both interfaces and the grids inside the artificial fluid. The equation of motion is then solved over the entire fluid domain to determine the displacement and velocity of the solid object. Ansys-CFX (1970-2017), is one of the commercial computational and engineering software packages in the market that has immersed boundary capabilities [12].

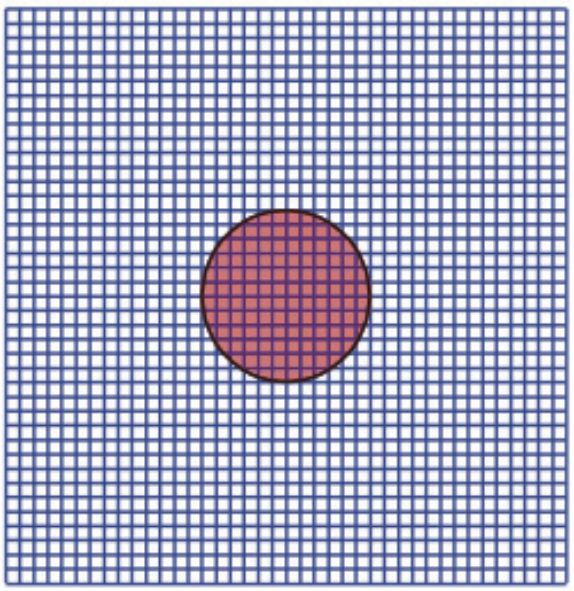

Figure 4.3: Immersed domain meshing

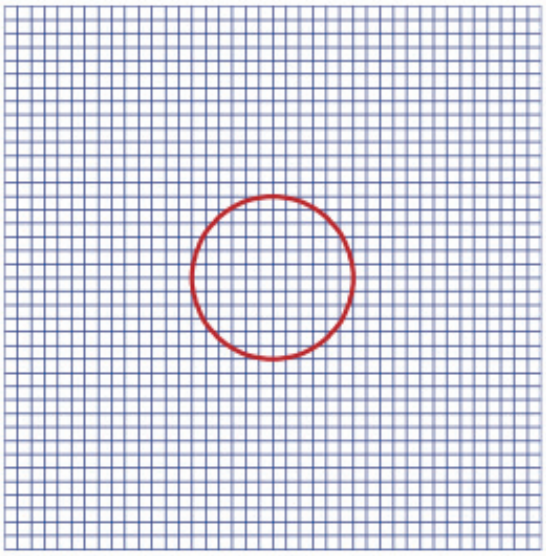

Figure 4.4: Immersed boundary meshing

4.1.4.2.3 Basic formulation of Immersed methods

We showed the equations that describe the motion for fluid structure interaction as:

$$\rho^s \dot{v_i}^f - \sigma^f_{ij,j} + f^f_i = 0 \qquad in \quad \overline{\Omega_f}, \tag{42}$$

$$\rho^s \dot{v_i}^s - \sigma^s_{ij,j} + f^s_i = 0 \qquad in \quad \overline{\Omega_s}, \tag{43}$$

where ${f_i}^f$ and ${f_i}^s$ are external body forces such as gravity and buoyancy and

$${u_i}^s = {u_i}^f \qquad in \quad \Gamma_s, \tag{44}$$

which shows that the displacement must be equal along the interface. The no-slip condition imposed on the interface between these two domains is the result of time differentiation of the above equation

$${\dot{u}_i}^s = {\dot{u}_i}^f \qquad in \quad \Gamma_s, \tag{45}$$

$$\ddot{u_i}^s = \ddot{u_i}^f \qquad in \quad \Gamma_s \tag{46}$$

Or, in terms of velocities:

$$v_i{}^s = v_i{}^f \qquad in \quad \Gamma_s, \tag{47}$$

$$\dot{v_i}^s = \dot{v_i}^f \qquad in \quad \Gamma_s. \tag{48}$$

Using Lagrangian multipliers we can combine the equations to [34]:

$$\begin{aligned} 0 = & \int_{\overline{\Omega_s}} (\rho^s \dot{v_i}^s - \sigma_{ij,j}{}^s + f_i{}^s) \delta u_i{}^s dv_i{}^s \\ & + \int_{\overline{\Omega_f}} (\rho^f \dot{v_i}^f - \sigma_{ij,j}{}^f + f_i{}^f) \delta u_i{}^f dv_i{}^f + \int_{\Gamma_s} \overline{\lambda_i} (\delta u_i{}^s - \delta u_i{}^f) dv_i, \end{aligned} \tag{49}$$

where $\overline{\lambda_i}$ is the Lagrange multiplier, and shows the fluid-structure interaction force. It has to be mentioned that the location of the interface boundary, Γ_s, is unknown, and its position is determined by the interaction between the fluid and the solid body.

In the original formulation of the immersed boundary method of Peskin [36], the structure is represented by an immersed boundary which is not represented by a finite volume. Thus we have $\overline{\Omega_s} = \Gamma_s$ and the fluid domain becomes the entire computational domain: $\Omega = \Omega_f$. Consequently, the above equation becomes:

$$0 = \int_{\Gamma_s} (\rho^f \dot{v_i}^s - \sigma_{ij,j}{}^s + f_i{}^s + \overline{\lambda_i}) \delta u_i{}^s dv_i + \int_{\Omega} (\rho^f \dot{v_i}^f - \sigma_{ij,j}{}^f + f_i{}^f + \overline{\lambda_i} L(\Gamma_s)) \delta u_i{}^f dv_i, \tag{50}$$

where the delta function, $L(\Gamma_s)$, is defined as:

$$L(\Gamma_s) = \begin{cases} 1 & \text{if } x \in \Gamma_s \\ 0 & \text{if } x \notin \Gamma_s \end{cases}$$

So two different equations can be derived as:

$$\rho^f \dot{v_i}^s - \sigma_{ij,j}{}^s + f_i{}^s + \overline{\lambda_i} = 0 \qquad on \quad \Gamma_s, \tag{51}$$

$$\rho^f \dot{v_i}^f - \sigma_{ij,j}{}^f + f_i{}^f + \overline{\lambda_i} L(\Gamma_s) = 0 \qquad in \quad \Omega. \tag{52}$$

In the immersed boundary method, the fluid-structure interaction force (the Lagrange multiplier $\overline{\lambda_i}$) is computed explicitly in Equation (51). The computed force is imposed to Equation (52), which is solved to give the fluid motion. In a numerical method, the discontinuous function $L(\Gamma_s)$ can be replaced by a continuous discrete delta function. The use of a discrete delta function is in fact an interpolation of the fluid structure force from the immersed boundary (the solid domain) to the fluid domain [36].

When the fluid velocity is solved, the velocity of the structure is determined by applying the no-slip condition. The same discrete delta function is usually used to interpolate the velocity from the fluid domain to the boundary. The location of the boundary Γ_s is then updated by using the solid displacement and velocity, and then used in the next time steps.

4.2 Ansys-CFX

4.2.1 Introduction to the CFX package

CFX is one of the packages in the ANSYS workbench in which the immersed boundary method has been implemented. Actually, Ansys-CFX supports both conforming and non-conforming mesh methods for fluid-structure interaction. However, since it has an immersed boundary solver, in this study, it is decided to use the non-conforming method (immersed boundary method) solver due to its flexibility and to avoid complicated mesh deformation equations and computational cost.

The immersed boundary method in CFX allows us to model steady state or unsteady simulations with rigid solid objects that can move through fluid domains. During the solution, CFX applies the fluid structure interaction force terms in the fluid conservation of momentum equation in order to force the flow to move with the solid. Based on the Ansys-CFX users guide [12], the steps to create an immersed solid in CFX are:

- *"Define an immersed solid domain to represent the solid. This domain should be entirely or partly within a fluid domain. Care must be taken to ensure that the immersed solid domain does not cross any fluid boundaries or collide with any solid domains or immersed solid domains. An immersed solid domain should not cross any interface that involves a non-stationary domain. Thus, there should not be a domain interface between the immersed solid domain and the fluid domain.*
- *Specify the domain motion settings for the immersed solid domain in order to prescribe the motion of the immersed solid."*

In CFX, fluid structure interaction is represented in the fluid equation as a source term that makes the fluid particles around the solid object take its velocity (no-slip condition). This source term is always controlled by a scaling factor which is set before the solution is initialized (in the "global control settings"). The default value of this scaling factor is usually equal to 10, which is used in this study.

4.3 Setup

4.3.1 Geometry

We use a simple geometry in this thesis, based on the experiments in a simple three dimensional geometry. A hexahedral domain with dimension $0.25 - 0.25 - 0.25$ meters was used. This domain was filled with tap water and spheres were released from a height of 0.195 meters ($\frac{x}{D} = 39$). Figure 4.5 shows the geometry defined for the CFD simulation. Based on the trajectory of the spheres in experiments, we define a cylindrical area inside the box as body of influence, where the grids is finer.

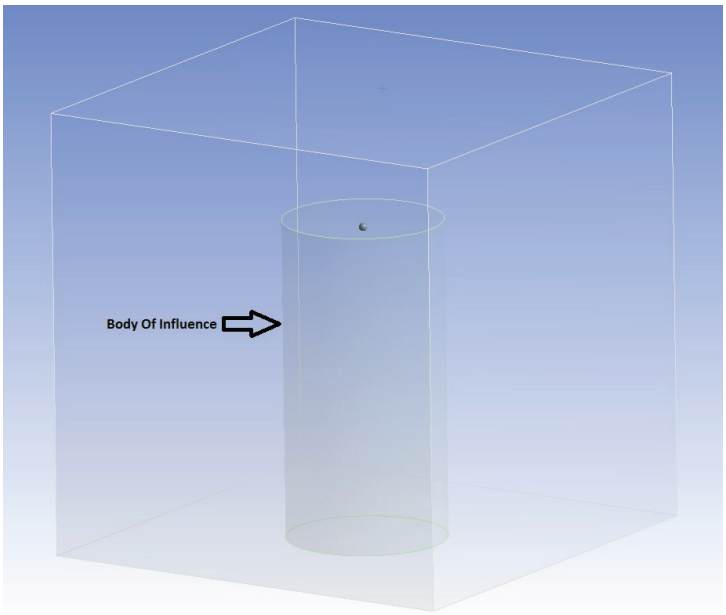

Figure 4.5: Geometry for CFD simulation

4.3.2 Meshing

4.3.2.1 Method of meshing

In order to have a comprehensive mesh on the whole domain we used the block decomposition method. A cylinder was assumed to be the predicted trajectory of the solid sphere where the meshing is tetrahedral unstructured. It is decided to use tetrahedral shaped

mesh outside of this body of influence as well. The algorithm for the unstructured meshing is chosen to be the "Delauney" method. The solid domain (spheres) has also unstructured tetrahedral shaped meshing.

4.3.2.2 Mesh size

Mesh size is an important factor in stability and accuracy of any CFD simulation. In fluid structure problems, in addition to this usual importance, mesh size plays an important role in the determining the fluid structure force and consequently in the investigation of solid object displacement, velocity, and acceleration. It becomes more crucial in the case of complex geometries or complex interfaces between a solid object and the fluid domain. The mesh size also becomes more stringent in the case of high Reynolds numbers or in the case of compressible high Mach number flows. A lot has been written about appropriate mesh size for FSI problems. For example, Glowinski et al. (1999) [39] in finite element analysis proved that the fluid mesh size, should equal to the solid object mesh size.
In another study, Zhao et al. (2008) [40] investigated using fluid structure methods in biological systems in which the immersed solid object is flexible. Their results showed that deformation in the interface of the solid and fluid domains can cause large inaccuracies in the simulation. In order to overcome this, they proposed that very fine meshes be used in the areas that could be in the trajectory of the solid object.
In this study, based on our rigid body assumption, we defined a cylindrical shape body of influence in the cubic fluid domain and we decided to have grid size of $0.000001\ m$ in the region of influence and growth rate of 12 percent outside of the region of influence. For the solid domain, we decide to have a grid size equal or less than $0.00001\ m$. Figures 4.6, and 4.7 shows the bottom and front view of the mesh generated for CFD simulation respectively.

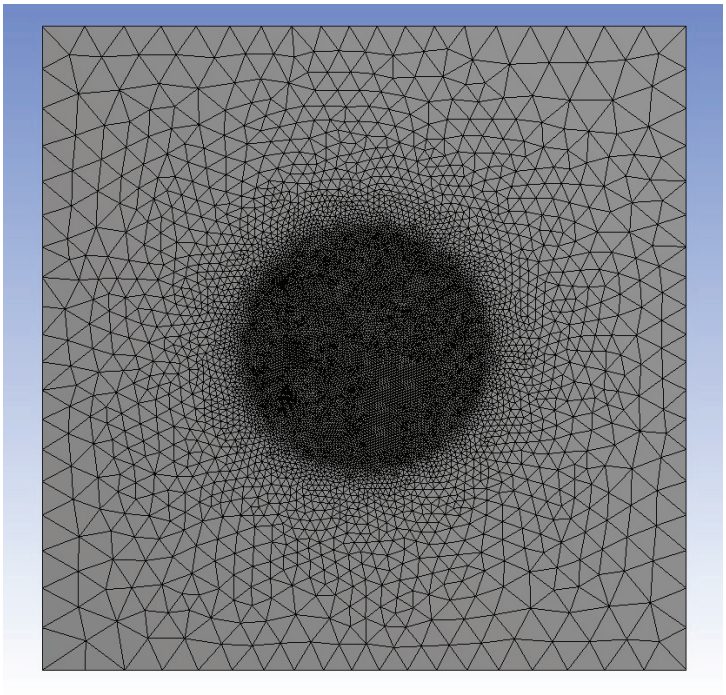

Figure 4.6: Bottom view of the mesh

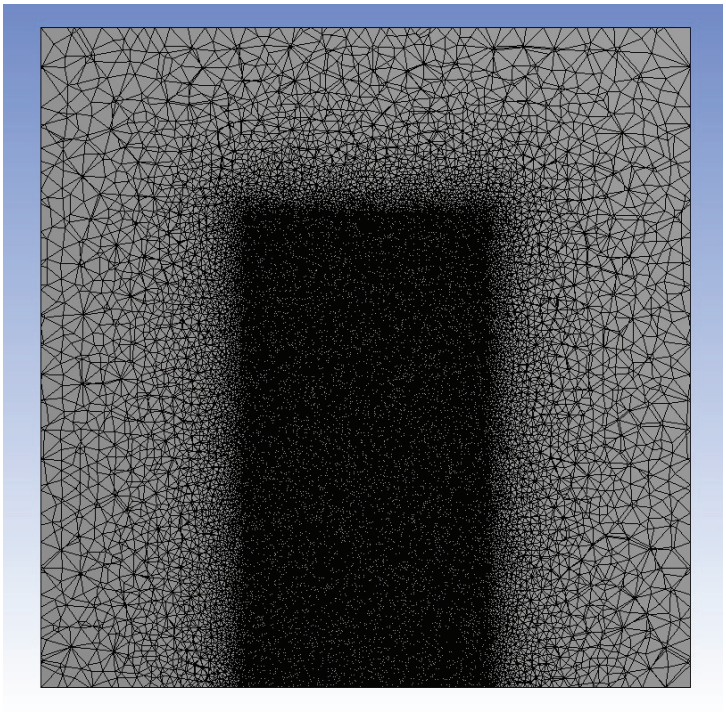

Figure 4.7: Front view of the mesh

4.3.3 Physical setup

4.3.3.1 Physical quantities of structure

As noted in the experimental and numerical solution chapters, we decided to use three different spherical shaped materials with their physical properties listed in Table (4.1).

Material	Density $\frac{\mathrm{Kg}}{\mathrm{m}^3}$	Volume m^3	Mass moment of Inertia Kgm^2
Delerin	1359.41	5.24e-7	7.12e-9
Teflon	2299.62	5.24e-7	1.205e-8
Steel	7779.19	5.24e-7	4.076e-8

Table 4.1: Physical quantities of the materials

4.3.3.2 Turbulence model

It is obvious that sedimentation of a sphere in a fluid creates a turbulent wake. So, in order to do a simulation we should first appropriately model this turbulence. In our case, we decided to use the Spalart-Allmaras model because it is known due to have high accuracy in aerodynamics applications and in this case the drag force plays an important role in the terminal velocity [41]. Spalart-Allmaras is a one-equation turbulence model, that has been developed mainly for aerodynamic flows, and is a transport equation for eddy viscosity. While other turbulence models exist, such as $k-\epsilon$, $k-\omega$, and etc. A study on the influence of turbulence model choice is beyond the scope of the current study. Therefore, we propose such a study as a recommendation for future works.

4.3.3.2.1 Governing equations

In addition to the rigid body dynamics, which are derived from Newton's second law and explains the dynamics of our solid sphere (three rotation equations and three translation equations), we have the fluid domain which has to be defined by using the continuity and

Navier-Stokes Equations. These governing equations using Einstein tensor notation are:

$$\frac{\partial \rho}{\partial t} + \frac{\partial}{\partial x_j}\left[\rho u_j\right] = 0, \tag{53}$$

$$\frac{\partial}{\partial t}\left(\rho u_i\right) + \frac{\partial}{\partial x_j}\left[\rho u_i u_j + p\delta_{ij} - \tau_{ji}\right] = 0, \quad i = 1, 2, 3. \tag{54}$$

In this case, we are dealing with water as an incompressible fluid. In the simulation we are modeling turbulence and are going to use the Spalart-Allmaras model. In this model, we need to take a time-average from the Navier-Stokes equations. First we use Reynold's decomposition to decompose all the quantities to average and fluctuation as follows [42]:

$$\phi = \overline{\phi} + \phi', \tag{55}$$

where:

$$\overline{\Phi} \equiv \frac{1}{T}\int_T \Phi(t)dt. \tag{56}$$

Then we take time average from the Navier-Stokes equations to obtain Reynolds Average Navier-Stokes (RANS) equations.

$$\rho(\frac{\partial \overline{u_i}}{\partial t} + \overline{u}_j\frac{\partial \overline{u_i}}{\partial x_j}) = -\frac{\partial \overline{P}}{\partial x_j} + \mu\frac{\partial^2 \overline{u_i}}{\partial x_j \partial x_j} + \frac{\partial \tau_{ij}}{\partial x_j}, \tag{57}$$

It can be seen that the τ_{ij} are new unknowns in our equation. we cannot solve this equation without additional assumptions. Based on assumption of the isotropy of turbulence we use the Boussinesq approximation as follows [42]:

$$\tau_{ij} = 2\,\mu_t\,S^*_{ij} - \frac{2}{3}k\delta_{ij}, \tag{58}$$

or more explicitly:

$$-\rho\overline{u_i' u_j'} = \mu_t\left(\frac{\partial \overline{u_i}}{\partial x_j} + \frac{\partial \overline{u_j}}{\partial x_i}\right) - \frac{2}{3}k\delta_{ij}. \tag{59}$$

in order to solve this equation, concept of dynamic eddy viscosity μ_t or kinematic eddy

viscosity ν_t has ben introduced. In order to determine this new term we have to make additional assumptions or solve new partial differential equations [41]. The Spalart-Allmaras model, often called the one-equation model, consists of one PDE of turbulent kinetic energy, which is derived by multiplying velocity fluctuation in the RANS:

$$\frac{\partial k}{\partial t} + \overline{u_j}\frac{\partial k}{\partial x_i} = -\overline{u_i' u_j'}\frac{\partial \overline{u_i}}{\partial x_j} - \nu\overline{\frac{\partial u_i'}{\partial x_j}\frac{\partial u_i'}{\partial x_j}} - \frac{1}{\rho}\frac{\partial}{\partial x_j}(\overline{u_j' p'}) + \nu\frac{\partial^2 k}{\partial x_j^2} - \frac{1}{2}\frac{\partial}{\partial x_j}(\overline{u_i' u_i' u_j'}), \tag{60}$$

We make an assumption which is called the Prandtl mixing length hypothesis and is proportional to the distance to the wall. This assumption helps us to find a relationship for eddy viscosity in equation (57).

$$\nu_t = l_m|\frac{\partial \overline{u_i}}{\partial x_j}|, \tag{61}$$

where l_m is Prandtl mixing length and depends on nature of the flow.
After mathematical manipulation we obtain the Spalart-Allmaras model:

$$\begin{aligned}\frac{\partial \tilde{\nu}}{\partial t} + u_j\frac{\partial \tilde{\nu}}{\partial x_j} &= C_{b1}[1 - f_{t2}]\tilde{S}\tilde{\nu} \\ &+ \frac{1}{\sigma}\{\nabla\cdot[(\nu+\tilde{\nu})\nabla\tilde{\nu}] + C_{b2}|\nabla\tilde{\nu}|^2\} - [C_{w1}f_w - \frac{C_{b1}}{\kappa^2}f_{t2}](\frac{\tilde{\nu}}{d})^2 + f_{t1}\Delta U^2,\end{aligned} \tag{62}$$

$$\nu_t = \tilde{\nu}f_{v1}, \quad f_{v1} = \frac{\chi^3}{\chi^3 + C_{v1}^3}, \quad \chi := \frac{\tilde{\nu}}{\nu}, \tilde{S} \equiv S + \frac{\tilde{\nu}}{\kappa^2 d^2}f_{v2}, \quad f_{v2} = 1 - \frac{\chi}{1+\chi f_{v1}}, \tag{63}$$

where:

$$S =\equiv \sqrt{2\Omega_{ij}\Omega_{ij}}, \tag{64}$$

$$\Omega_{ij} \equiv \frac{1}{2}(\frac{\partial u_i}{\partial x_j} - \frac{\partial u_j}{\partial x_i}), \tag{65}$$

$$f_w = g\left[\frac{1+C_{w3}^6}{g^6 + C_{w3}^6}\right]^{1/6}, \quad g = r + C_{w2}(r^6 - r), \quad r \equiv \frac{\tilde{\nu}}{\tilde{S}\kappa^2 d^2}, \tag{66}$$

$$f_{t1} = C_{t1} g_t \exp(-C_{t2} \frac{\omega_t^2}{\Delta U^2}[d^2 + g_t^2 d_t^2]), \tag{67}$$

$$f_{t2} = C_{t3} \exp(-C_{t4} \chi^2), \tag{68}$$

where d is the distance to the closest surface and the constants are:

$$\begin{aligned}
\sigma &= 2/3, \\
C_{b1} &= 0.1355, \\
C_{b2} &= 0.622, \\
\kappa &= 0.41, \\
C_{w1} &= C_{b1}/\kappa^2 + (1 + C_{b2})/\sigma, \\
C_{w2} &= 0.3, \\
C_{w3} &= 2, \\
C_{v1} &= 7.1, \\
C_{t1} &= 1, \\
C_{t2} &= 2, \\
C_{t3} &= 1.1, \\
C_{t4} &= 2.
\end{aligned}$$

4.3.3.3 Boundary conditions

Due to having quiescent fluid (water) in a box, defining the boundaries is simple. We have no-slip condition on five surfaces of the box at the bottom and the sides and we just have one free-slip condition at the top of the box. we have also a wall condition (no-slip condition) on the surface of the solid sphere where the solid body and the fluid interact.

4.3.3.4 Initial condition

At time zero, we have quiescent water so the water velocity is zero and water pressure is hydro-static pressure. The solid sphere is also stationary as shown in Figure (4.8). Characterisitic pressure is defined as $P' = \frac{m}{Dt'^2}$ and consequently, dimensionless pressure as $\frac{P}{P'}$, where P is hydrostatic pressure.

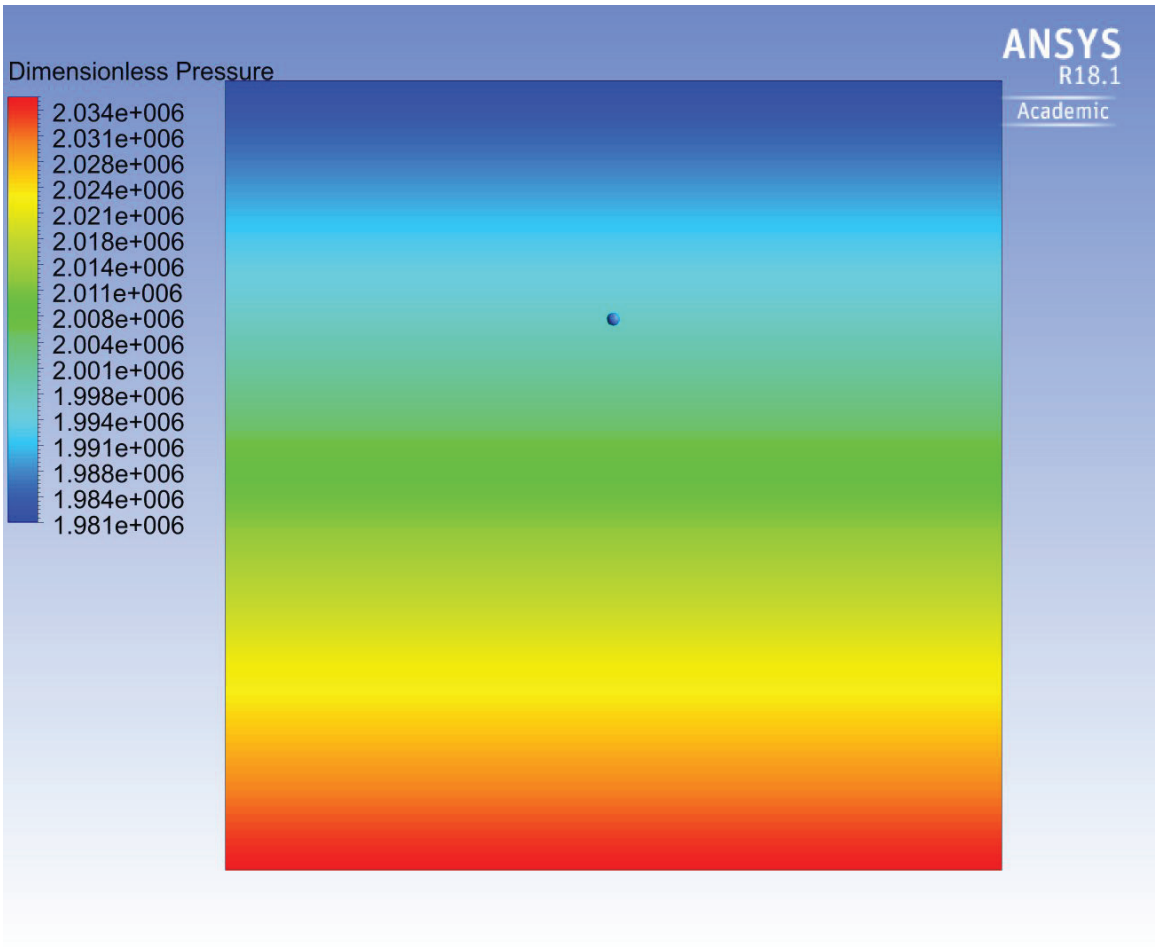

Figure 4.8: Hydrostatic pressure at $t/t' = 0$

4.3.4 Time steps and time integration

As was mentioned previously, in this simulation we decided to use a URANS model (Unsteady Reynolds Average Navier-Stokes). It is typically assumed that a time-average

model has to be steady state. However, in Equation (57) we can retain the transient term $\frac{\partial \overline{u_i}}{\partial t}$ so by convention we call it a URANS approach. As discussed earlier, the averaged components are still a function of time. Therefore the results from the URANS are unsteady, but one is often interested only in the time-averaged flow. Here the time-averaged velocity and fluctuating velocity means that we decomposed the results from Navier-Stokes equations as a time-averaged part and a resolved turbulent fluctuation, which are both time dependent.

Another challenge in maintaining accuracy and stability of any CFD simulation is time step size. Generally, time discretizations can be categorized as implicit or explicit schemes. However, in a fluid structure interaction problem, since we are dealing with movement of a solid object through the fluid, numerical stability can be improved by using implicit and semi-implicit time discretization. The fully implicit and semi-implicit time integration of the immersed boundary methods typically contains computation of a large system of coupled equations via a large number of iterations, which has to be converged. However, semi-implicit methods have reduced computational cost in comparison to fully implicit ones. Semi-implicit schemes in fluid structure interaction were first developed by Peskin [36] and later was proved by Newren (2008) [43] that is unconditionally stable in first and second order conditions so we can say that semi-implicit schemes have an acceptable order of accuracy and stability for our study.

In this study, since the simulation was running in parallel on a 2nd generation Intel Core i7 cpu which has four cores and four threads. Due to memory requirements, a fully implicit solution was impossible. Hence we decided to use semi-implicit time schemes for our simulation.

4.3.5 Numerical schemes

With respect to time step and mesh size and for higher accuracy we used the following schemes as shown in Table (4.2).

Entity	Scheme
Temporal	Second order backward Euler
Spatial	Second order upwind
Laplacian	Gauss linear
Interpolation	Linear

Table 4.2: Schemes used in the simulation

Second order backward Euler is a semi-implicit time discretization which is defined as:

$$u(x, t_{n+1}) = u(x, t_n) + \frac{\partial u(x, t_{n+1})}{\partial t}\Delta t + \frac{\partial^2 u(x, t_{n+1})}{\partial t^2}\frac{\Delta t^2}{2} \tag{69}$$

In CFX second order upwind spatial scheme is an improvement of first order upwind scheme by including 3 points instead of just 2. In this approach, higher-order accuracy is achieved at cell faces through a Taylor series expansion. In this method the face value Φ_f is computed by:

$$\Phi_f = \Phi + \nabla\Phi \cdot \vec{r}, \tag{70}$$

where Φ and $\nabla\Phi$ are the cell-centered value and its gradient in the upstream cell, and $\vec{r}$ is the displacement vector from the upstream cell centroid to the face [12].

And Gauss linear laplacian for a grid size of h in one dimension can be defined as:

$$\nabla^2\Psi = \frac{\partial^2\Psi}{\partial x^2} = \frac{\Psi_{n+1} - 2\Psi_n + \Psi_{n-1}}{h^2} - \frac{h^2}{12}(\frac{\partial^4\Psi}{\partial x^4}), \tag{71}$$

where Ψ is an arbitrary scalar field.

4.4 CFD simulation results

4.4.1 Impact quantities

In Table (4.3) the CFD dimensionless impact velocity, time, and Reynolds Number for three different density ratios are shown.

Sphere Material	$\frac{\rho_s}{\rho_f}$	$\frac{h}{D}$ falling height	$\frac{V_i}{V'}$ impact velocity	$\frac{t_i}{t'}$ impact time	Re_{p_i}
Delrin	1.394	39	0.692	31.72	1085
Teflon	2.304	39	1.33	17.53	2085
Steel	7.794	39	3.37	8.54	5260

Table 4.3: Results from free fall of three density ratios based on CFD approach

4.4.2 Numerical simulation curves

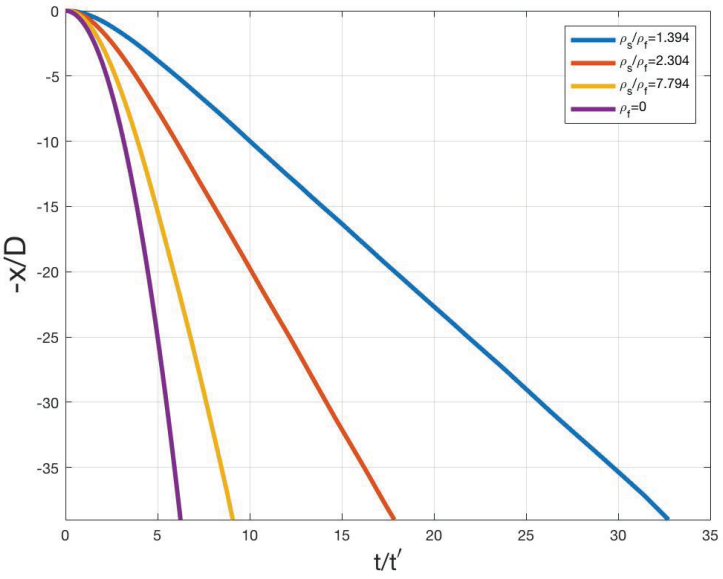

Figure 4.9: Dimensionless displacement curves by CFD

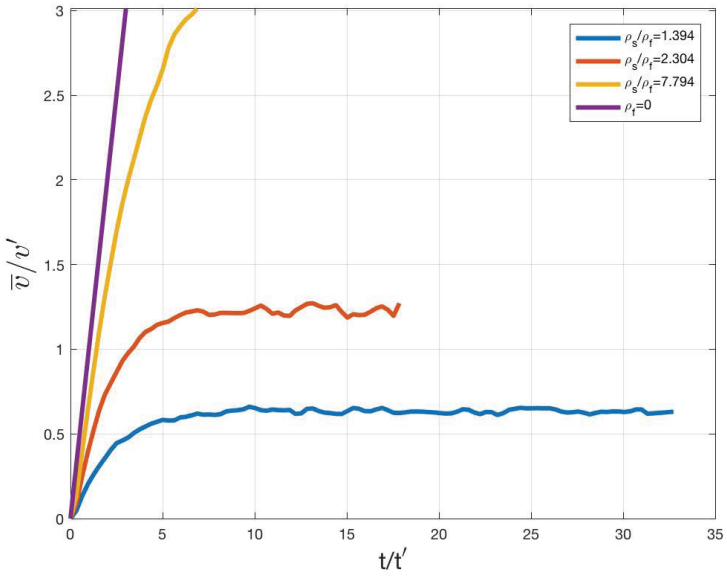

Figure 4.10: Dimensionless velocity curves by CFD

In Figures 4.9 and 4.10, dimensionless graph of position and velocity for different density ratios can be seen. These two graphs and Table 4.3 show that as density ratio (mass ratio) increases the terminal velocity increases and the sphere reaches to ground faster as its corresponding displacement and velocity curves approach to the displacement and velocity curve in vacuum condition.

In the velocity curves 4.10, the oscillations can be observed. These oscillations are believed to be associated with turbulent effect. This chaotic turbulent behavior causes instability in the motion of the spheres.

4.4.3 Velocity, pressure and vorticity contours

The velocity contours around the spheres at dimensionless height of $x/D = 37.02$ for individual density ratios ($\rho_s/\rho_f = 1.394$, $\rho_s/\rho_f = 2.304$, and $\rho_s/\rho_f = 7.794$) are plotted in Figures 4.11a, 4.11c and 4.11e. As it was expected an area of high velocity is observed in the top of the spheres. This high velocity caused by the circulation bubbles around the spheres. However, the velocity decreases with distance from the top of the spheres in downstream.

An area of high pressure can be detected in the bottom of the spheres. This area has a higher pressure as the density of the spheres increases. An area of low pressure in the sides and a relatively high pressure region can be observed in the wake of the spheres.

More details about movement of spheres are observed by looking at the vorticity contours in Figures 4.11b, 4.11d and 4.11d at dimensionless height of $x/D = 37.02$. The higher vorticity can be interpreted as a large region of rotational flow. Rotational flow is very common in viscous flows, specially in the boundary layer where an inhomogeneous normal derivative of the velocity component is observed. Therefore, as it was expected, high vorticity regions are the boundary layer around the spheres and the maximum value of vorticity happens in a thin layer near the wall of spheres (boundary layer). High values are also observed in separated boundary region, as well as inside a viscous vortex.

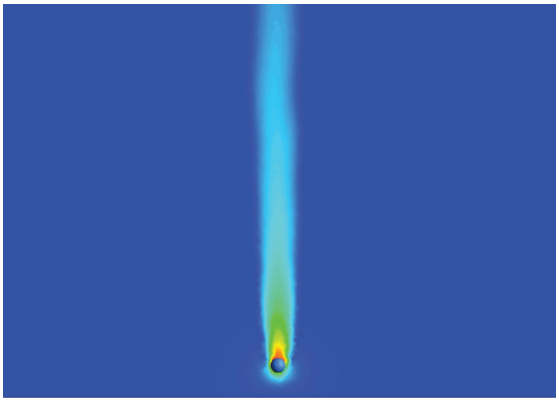

(a) Velocity contours at $x/D = 37.02$ for $\rho_s/\rho_f = 1.394$ (Delerin)

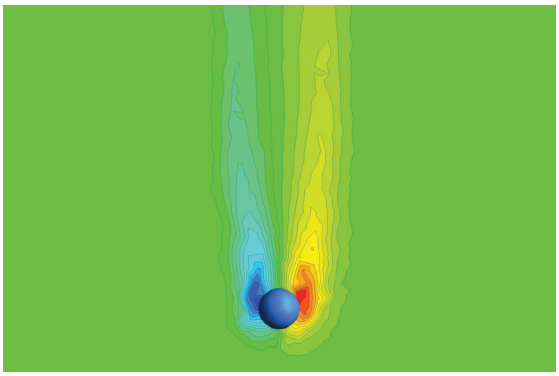

(b) Vorticity contour at $x/D = 37.02$ for $\rho_s/\rho_f = 1.394$ (Delerin)

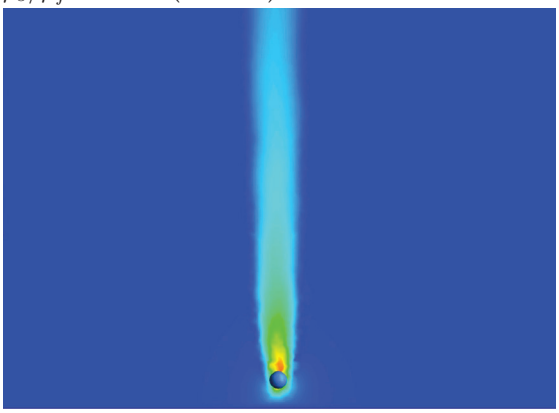

(c) Velocity contour at $x/D = 37.02$ for $\rho_s/\rho_f = 2.304$(Teflon)

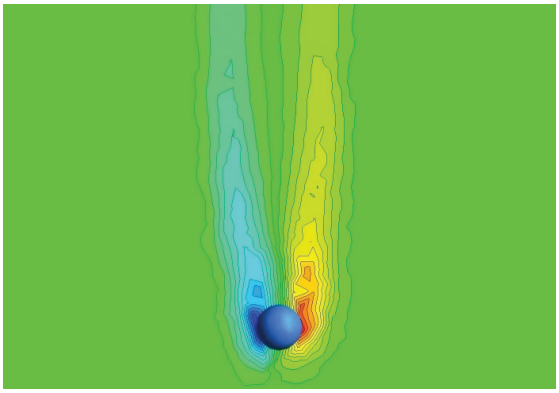

(d) Vorticity contour at $x/D = 37.02$ for $\rho_s/\rho_f = 2.304$ (Teflon)

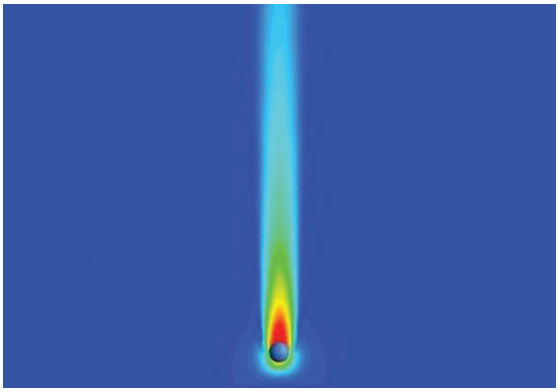

(e) Velocity curve at $x/D = 37.02$ for $\rho_s/\rho_f = 7.794$ (steel)

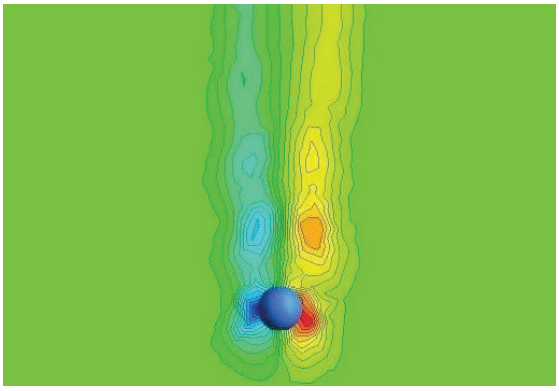

(f) Vorticity contour at $x/D = 37.02$ for $\rho_s/\rho_f = 7.794$ (steel)

Figure 4.11: Velocity and vorticity contours

4.4.4 Q-criterion isosurfaces

Turbulent flow is considered as a full 3-dimensional phenomena. However, showing the turbulence structure is not easy. Hence, a parameter (Q-criterion) is defined to represent the turbulent structure. Q-criterion is defined as second invariant of velocity gradient tensor. Q-criterion is also defined as difference of vorticity and strain tensor.

$$Q = \frac{1}{2}(||\omega|| - ||S||), \tag{72}$$

where ω is vorticity tensor and S is the symmetric strain rate.

In Figures (4.12a), (4.12b) and (4.12c), isosurfaces of Q-criterion = 100 are shown. It is believed that instability in the movement of the spheres is associated to these turbulent structures [9]. In other words, the oscillations which were observed in the velocity curve of the spheres are associated to these turbulent structures. However, future work is needed to study their influence in more detail.

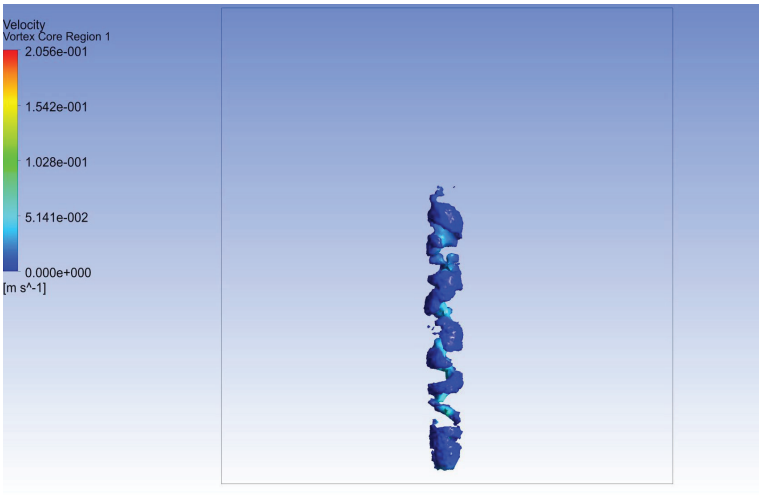

(a) Delerin sphere $\rho_s/\rho_f = 1.394$ at $x/D = 37.02$

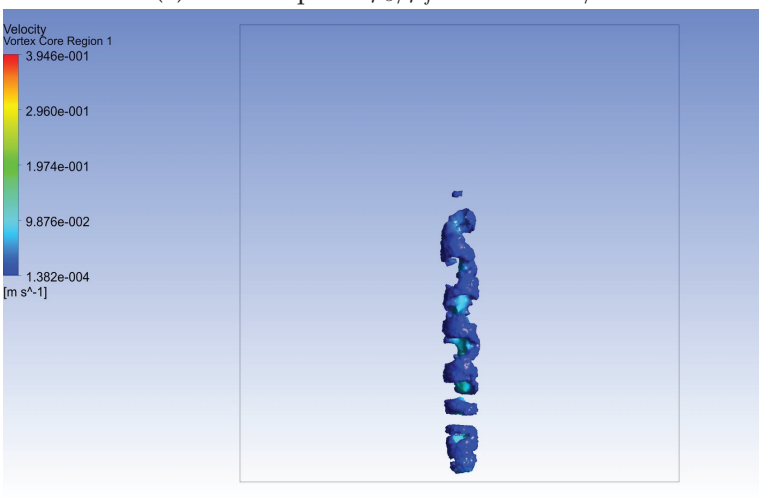

(b) Teflon sphere $\rho_s/\rho_f = 2.304$ at $x/D = 37.02$

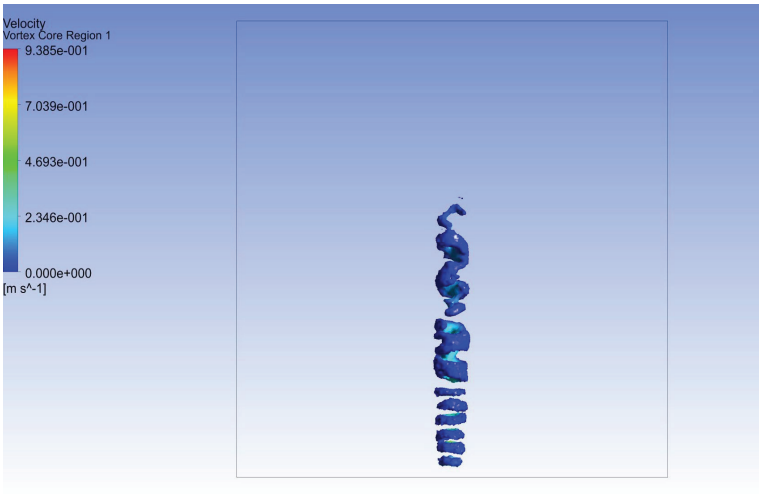

(c) Steel sphere $\rho_s/\rho_f = 7.794$ at $x/D = 37.02$

Figure 4.12: Isosurfaces of Q-criterion = 100

Chapter 5

Comparison and Conclusion

5.1 Comparison

In Figures 5.1a, 5.1c, and 5.1e dimensionless displacement curves based on experimental data and numerical solution of the BBO equation for different density ratios ($\rho_s/\rho_f = 1.394$, $\rho_s/\rho_f = 2.304$, and $\rho_s/\rho_f = 7.794$) are plotted and Figures 5.1b, 5.1d, and 5.1f represent corresponding difference in displacement curves based on numerical solution of BBO equation and experimental data. As it can be drawn from these figures, we can see that difference is very low in the beginning. However, since the predicted terminal velocity in the two approaches is different, the difference in predicted location increases as time passing and it reaches about 1 (difference$/D = 1$) after falling for a dimensionless height (x/D) of 39. oscillations are also seen in the difference curves, these oscillation are associated to fluctuation in experimental curves which are related to turbulent effect (turbulent wake). Figures 5.2a, 5.2c, and 5.2e show dimensionless displacement curves based on CFD simulation and numerical solution of the BBO equation for different density ratios ($\rho_s/\rho_f = 1.394$, $\rho_s/\rho_f = 2.304$, and $\rho_s/\rho_f = 7.794$), and Figures 5.1b, 5.1d, and 5.1f show corresponding difference in displacement curves based on numerical solution of BBO equation and experimental data. In these figures we can see approximately the same trend we saw in comparison of numerical solution and experimental data. The difference is relatively low

in the beginning but it increases as the spheres fall through the fluid. However, in comparison of CFD and experimental data the amplitude of oscillation is much smaller. This small amplitude of oscillation can be explained with the fact that RANS turbulence modelling which uses a time average statistical approach. Consequently, the turbulent fluctuations are smoother in this model.

In a similar way, Figures 5.3a, 5.3c, and 5.3e demonstrate dimensionless displacement curve based on experimental data and CFD simulation for different density ratios ($\rho_s/\rho_f = 1.394$, $\rho_s/\rho_f = 2.304$, and $\rho_s/\rho_f = 7.794$), and Figures 5.1b, 5.1d, and 5.1f represent corresponding difference in displacement curve. These figures show lower difference between CFD and experimental curves, which remains relatively constant through the movement. However, high amplitude oscillation can be seen in difference curves. As it was described before, it is believed that these oscillations are associated to the turbulence effect in both experimental and CFD simulation.

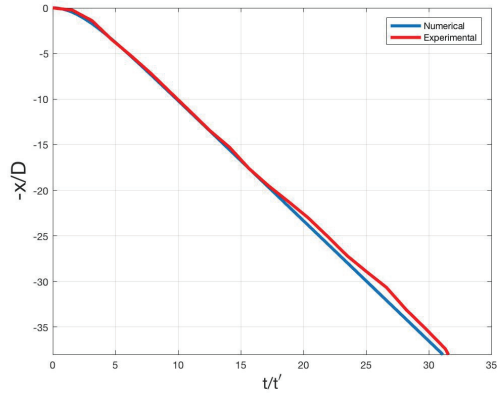

(a) Displacement curves for $\rho_s/\rho_f = 1.394$ (Delerin)

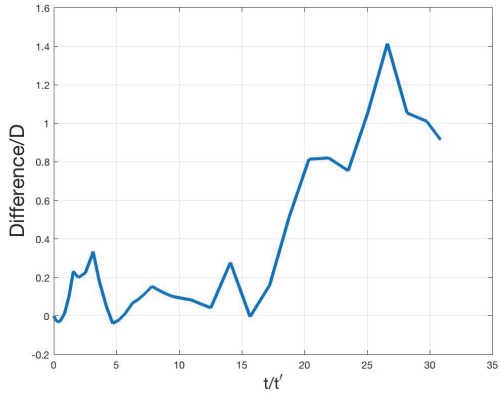

(b) Difference in position for $\rho_s/\rho_f = 1.394$ (Delerin)

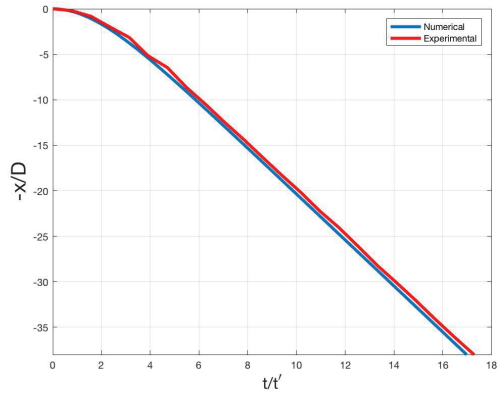

(c) Displacement curves for $\rho_s/\rho_f = 2.304$(Teflon)

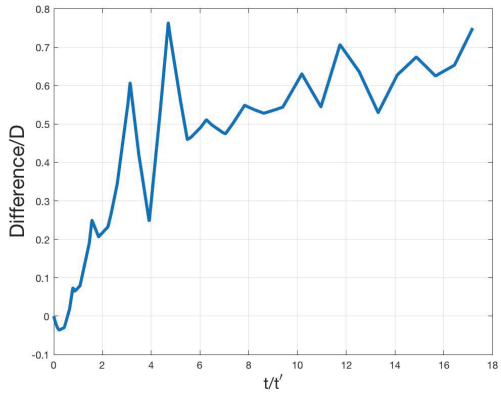

(d) Difference in position for $\rho_s/\rho_f = 2.304$ (Teflon)

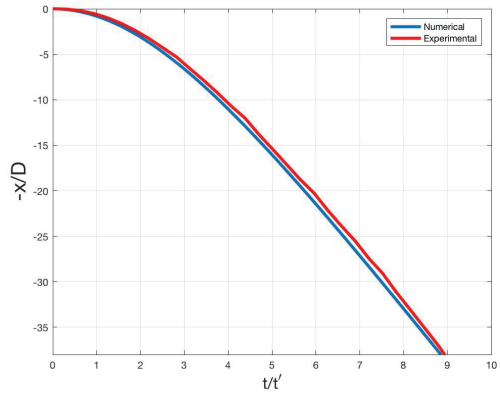

(e) Displacement curves for $\rho_s/\rho_f = 7.794$ (steel)

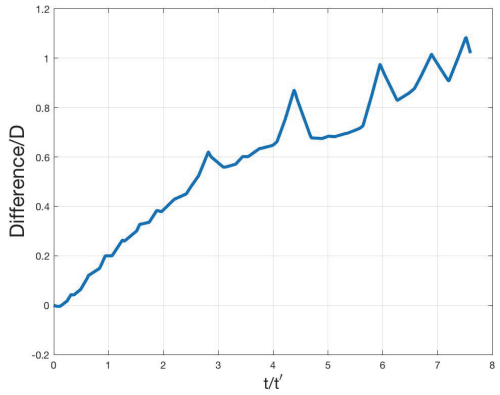

(f) Difference in position for $\rho_s/\rho_f = 7.794$ (steel)

Figure 5.1: Comparison between numerical simulation and experiments

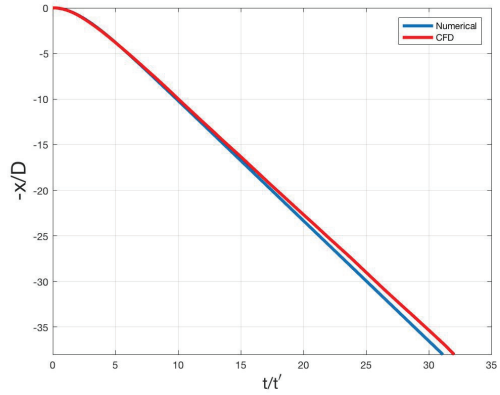

(a) Displacement curves for $\rho_s/\rho_f = 1.394$ (Delerin)

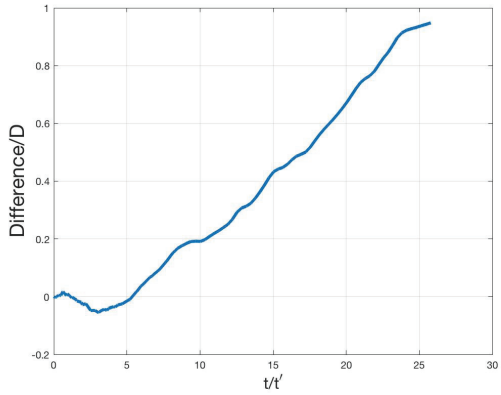

(b) Difference in position for $\rho_s/\rho_f = 1.394$ (Delerin)

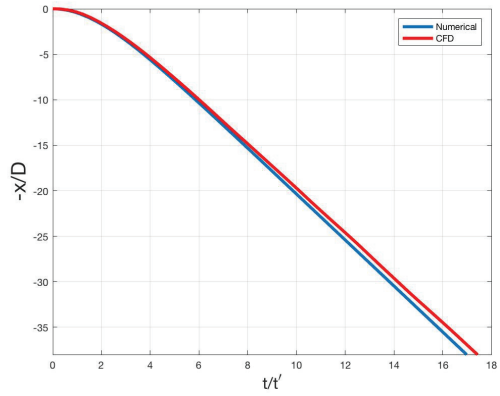

(c) Displacement curves for $\rho_s/\rho_f = 2.304$ (Teflon)

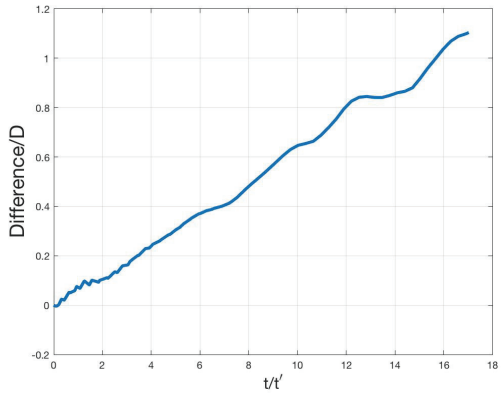

(d) Difference in position for $\rho_s/\rho_f = 2.304$ (Teflon)

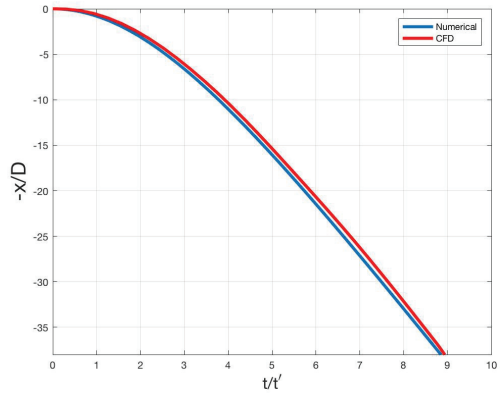

(e) Displacement curves for $\rho_s/\rho_f = 7.794$ (steel)

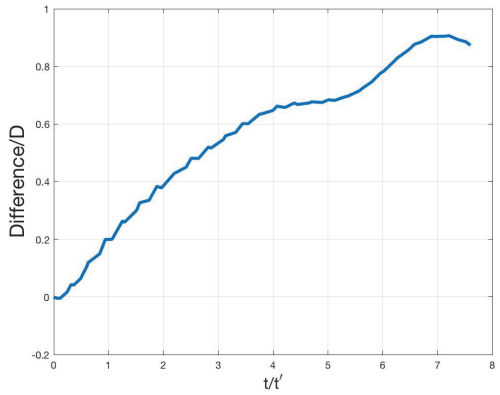

(f) Difference in position for $\rho_s/\rho_f = 7.794$ (steel)

Figure 5.2: Comparison between numerical simulation and CFD

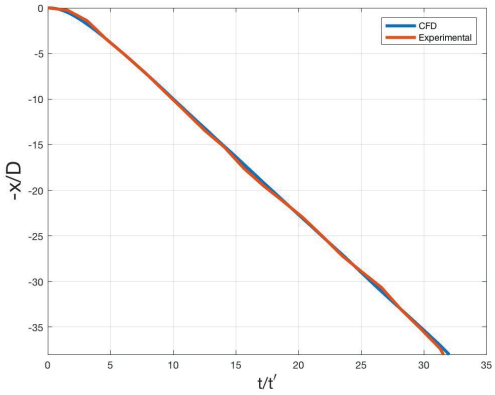

(a) Displacement curves for $\rho_s/\rho_f = 1.394$ (Delerin)

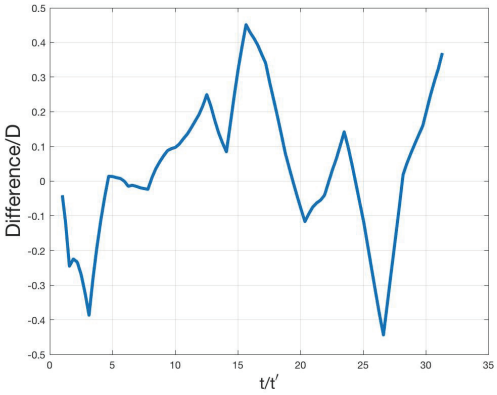

(b) Difference in position for $\rho_s/\rho_f = 1.394$ (Delerin)

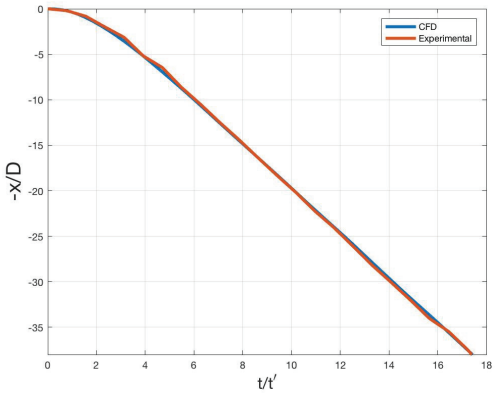

(c) Displacement curves for $\rho_s/\rho_f = 2.304$ (Teflon)

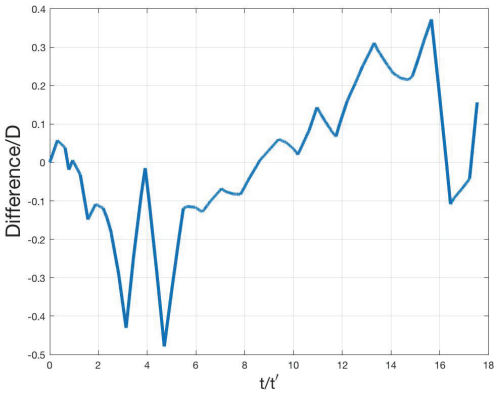

(d) Difference in position for $\rho_s/\rho_f = 1.394$ (Teflon)

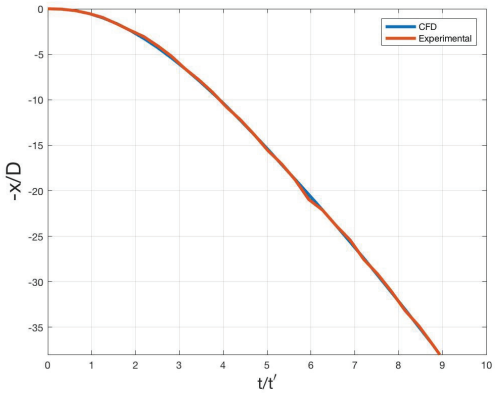

(e) Displacement curves for $\rho_s/\rho_f = 7.794$ (steel)

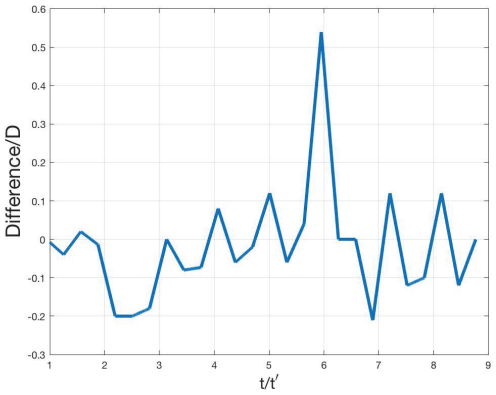

(f) Difference in position for $\rho_s/\rho_f = 7.794$ (steel)

Figure 5.3: Comparison between CFD and experiments

5.1.1 Comparison of impact quantities based on experimental, numerical solution, and CFD simulation

$\rho_s/\rho_f = 1.394$	t_i/t' impact time	V_i/V' impact velocity	Impact Reynolds number	Difference percentage in impact time prediction
Experiments	32.02	0.689	1075	0
Numerical	31.07	0.709	1100	2.96
CFD	31.72	0.692	1085	0.95

Table 5.1: Comparison of impact quantities based on experiments, numerical solution, and CFD for $\rho_s/\rho_f = 1.394$ (Delerin)

$\rho_s/\rho_f = 2.304$	t_i/t' impact time	V_i/V' impact velocity	Impact Reynolds number	Difference percentage in impact time prediction
Experiments	17.74	1.31	2045	0
Numerical	17.02	1.37	2140	4.05
CFD	17.53	1.33	2085	1.18

Table 5.2: Comparison of impact quantities based on experiments, numerical solution, and CFD for $\rho_s/\rho_f = 2.304$ (Teflon)

$\rho_s/\rho_f = 7.794$	t_i/t' impact time	V_i/V' impact velocity	Impact Reynolds number	Difference percentage in impact time prediction
Experiments	8.55	3.36	5245	0
Numerical	8.24	3.39	5295	3.62
CFD	8.54	3.37	5260	0.11

Table 5.3: Comparison of impact quantities based on experiments, numerical solution, and CFD for $\rho_s/\rho_f = 1.794$ (steel)

Tables 5.1, 5.2, and 5.3 show that there is a good agreement between our experimental observations and CFD simulations (0 to 2 percent difference). However, there is 2 to 5 percent difference in impact quantities in the numerical solution of equation of motion of solid spheres. Impact quantities are defined as sphere falls through a fluid for a dimensionless hight $x/D = 39$.

It is evident in comparison of these three tables that as density ratio increases, Reynolds number after a dimensionless displacement of $\frac{x}{D} = 39$ increases and it is clear that required time for such a dimensionless displacement decreases significantly.

5.2 Summary

In this dissertation, we first performed an experimental investigation of free fall through a fluid. Then by using the BBO formulation, we conducted a numerical solution of the equation of motion of free falling spheres. Furthermore, we conducted CFD simulations by using the fluid structure interaction (FSI) non-conforming mesh method. We finally made a comparison between data from the experimental, numerical and CFD studies and came to the general conclusion that in case of free falling objects through a fluid, where we are dealing with a nonlinear transient drag force, the numerical solution to the equation of motion gives a good approximation of displacement, velocity and forces. Nevertheless, these methods are limited to solid objects with simple shapes (such as spheres) and simple fluid motions. It also does not represent chaotic turbulent effects in the solid object motion. However, numerical simulation of the Navier-Stokes equations (CFD simulation), is able to represent both the solid object motion and the effect of its motion on the fluid.

5.3 Conclusion

- As can be observed from our experimental, numerical, and CFD results, it is demonstrated that heavier spheres reach the ground faster than lighter spheres. Therefore, we can say that Aristotle's quotes about the free fall of a solid object through a fluid had not been wrong. His claim was based on observation and experiments in air. However, Galileo talked only about free fall in a vacuum situation.
- We can conclude that the added (virtual) mass and history forces, which appear in the BBO equation, are transient terms, which are derived from unsteady terms in the Navier-Stokes equations. They resist acceleration, and, consequently, they decrease the rate of acceleration of the spheres.
- We can conclude from numerical solution of the BBO equation that effect of the history or basset forces is not more than 2 percent of the overall force. However, the

effect of added mass is significant.

- CFD simulation is a more reliable approach to study the free fall of solid objects through a quiescent fluid.

5.4 Recomendations for future works

In this study, we simulated free fall of spheres through a quiescent fluid demonstrating good agreement with experiments. However, an interesting study in the direction of this thesis would be to investigate the stability of falling spheres in a quiescent fluid. Another interesting research area would be to study the importance and effects of the history force on the bed impact time and impact velocity. Furthermore, we propose to simulate this case using conforming mesh methods like the arbitrary Lagrangian Eulerian methods (ALE). We also suggest a comprehensive study of the wakes behind the falling objects through fluids, since many studies including Rostami et al [9], [10], and [24] associate the oscillation in the velocity and acceleration (force) to turbulent vortex shedding behind the falling objects. A detailed study of these wakes would be interesting. Doing the same study with different dimensionless height, density ratios, and Reynolds numbers could also be a very interesting subject for the future investigations.

Appendix A

MATLAB CODE

```
% Siavash Hedayati Nasab 40012529 %
% Depatment of Mechanical and Industrial Engineering %
%-------------------------------------------------------------%
%clc,clear ,close all
global rho mu D rhos vo mt A m
rho=998.1; %kg per cubic meter
Tf=0.293;
rhos=7.794*rho; % kg per cubic meter
D=0.005; % sphere diameter per meter
A=0.25*pi*(D^2);  % Surface Area per square meter
vo=((4/3)*pi*0.125*(D^3));  % Volume of the Sphere per Cubic Meter
m=rhos*vo;% kg
mt=m+(0.5*rho*vo);
mu=1e-3; % Dynamic Viscosity Kg per Meter Second
h=0.195;
tspan=[0 Tf];   % Time Span
tspan2=[0 Tf];
tspan3=[0 Tf];
```

```
initial_v=-0.00001;
initial_x=[h initial_v];
[t1,x]=ode45(@kutta,tspan,initial_x);
[t2,y]=ode45(@drag,tspan2,initial_x);
[t3,z]=ode45(@history,tspan3,initial_x);
plot(t1,abs(x(:,2)),'b','LineWidth',3);
hold on;
plot(t2,abs(y(:,2)),'r','LineWidth',3);
hold on;
plot(t3,abs(z(:,2)),'g','LineWidth',3);
xlabel('Time(Seconds)');
ylabel('Velocity(Meter per Second)');
legend('Total force','Total force without added mass and history force');
grid;
%%%%%%%%%%%%%%%%%%%%%%%%%%%%%%%%%%%%%%%%%%%%%%%%%%%%%%%%
figure;
plot(t1,x(:,1),'b','LineWidth',3);
hold on;
plot(t2,y(:,1),'r','LineWidth',3);
hold on;
plot(t3,z(:,1),'g','LineWidth',3);
xlabel('Time(Seconds)');
ylabel('Displacement (Meter)');
ylim([0 0.2]);
legend('Total force','Total force without added mass and history force');
grid;
hold on;
plot(T,dis,'r','LineWidth',3);
legend('Numerical','Experimental');
```

```
xq=0:0.001:1.02;
xqa=interp1(T,dis,xq);
xqb=interp1(t1,x(:,1),xq);
dfr=(xqa-xqb).*1000;
plot(xq,dfr,'LineWidth',3);
grid;
xlabel('Time (Second)');
ylabel('Error (Milimeter)');
legend('Error between numerical and experimental results');
%%%%%%%%%%%%%%%%%%%FORCE%%%%%%%%%%%%%%%%%%%%%%%%%%%%%%
a_D=zeros(1,length(y));

for i=1:length(y)-2
    a_D(i+1)=(y(i+2,2)-y(i,2))./(t2(i+2)-t2(i));
end
a_D(1)=a_D(2);
a_D(length(y))=a_D(length(y)-1);
F_D=m.*(a_D);
figure;
plot(t2,F_D,'r','LineWidth',3);
xlabel('Time (Seconds)');
ylabel('Drag Force (Newton)');
grid;
hold on,

a_T=zeros(1,length(x));

for i=1:length(x)-2
    a_T(i+1)=(x(i+2,2)-x(i,2))./(t1(i+2)-t1(i));
```

```
end
a_T(1)=a_T(2);
a_T(length(x))=a_T(length(x)-1);
F_T=mt.*(a_T);
plot(t1,F_T,'b','LineWidth',3);

a_H=zeros(1,length(z));

for i=1:length(z)-2
    a_H(i+1)=(z(i+2,2)-z(i,2))./(t3(i+2)-t3(i));
end
a_H(1)=a_H(2);
a_H(length(z))=a_H(length(z)-1);
F_H=mt.*(a_H);
plot(t3,F_H,'g','LineWidth',3);
legend('Total force withput adde mass and history force','Total force');
```

Appendix B

Camera acA640-750um Specifications

General Information

Order Number	106748
Product Line	ace U

Sensor

Sensor Vendor	ON Semiconductor
Sensor	PYTHON 300
Shutter	Global Shutter
Max. Image Circle	1/4"
Sensor Type	CMOS
Sensor Size	3.1 mm x 2.3 mm
Resolution (H x V)	640 px x 480 px
Resolution	VGA
Pixel Size (H x V)	4.8 µm x 4.8 µm
Frame Rate	751 fps
Mono/ Color	Mono

EMVA Data

EMVA Quantum Efficiency (typical)	52.0 %
Dark Noise (typical)	10.5 e^-
Saturation Capacity (typical)	7.1 ke^-
Dynamic Range (typical)	56.6 dB

EMVA Data

Signal- to -Noise Ratio	38.5 dB

Camera Data

Interface	USB 3.0
Video Output Format	Mono 10 Mono 10 Packed Mono 8
Pixel Bit Depth	10 bits
Synchronization	software trigger hardware trigger free-run
Exposure Control	programmable via the camera API hardware trigger
Digital Input	1
Digital Output	1
General Purpose I/O	2
Power Requirements	Via USB 3.0 interface
Power Consumption (typical)	3 W

Housing

Housing Type	Box
Housing Size (L x W x H)	29.3 mm x 29 mm x 29 mm
Lens Mount	C-mount
Housing Temperature	0 - 50°C
Weight (typical)	80g

Conformity

Conformity	CE RoHS IP30 FCC USB3 Vision GenICam UL

Bibliography

[1] Aristotle. *"Physics" in The Works of Aristotle*. University of Chicago, 1990.

[2] Mario Rabinowitz. Falling bodies: the obvious, the subtle, and the wrong. *Power Engineering Review*, pages 27–31, 1990.

[3] John Urmson and Paul Lettinck. *Philoponus: On Aristotle Physics 5-8 with Simplicius: on Aristotle on the Void*. Bloomsbury Publishing, 2014.

[4] Stillman Drake. *Galileo at Work: His Scientific Biography*. Courier Corporation, 1978.

[5] Stillman Drake. *History of Free Fall: Aristotle to Galileo; with an Epilogue on "pi" in the Sky*. Wall & Emerson, 1989.

[6] Michael B Abbott and David R Basco. Computational fluid dynamics: an introduction for engineers. *NASA Technical Report A*, 90, 1989.

[7] https://www.britannica.com/science/cavitation Britannica Encyclopedia. Cavitation, 2010.

[8] https://www.rt.com/news/meteorite-crash-urals-chelyabinsk-283/ Russia Today. Meteorite explosion, 2013.

[9] Mohammad Rostami, Abdullah Ardeshir, Goodarz Ahmadi, and Peter Joerg Thomas. Can the history force be neglected for the motion of particles at high subcritical Reynolds number range. *International Journal of Engineering Transactions and Applications*, 19(1):23, 2006.

[10] Mohammad Rostami, Abdullah Ardeshir, Goodarz Ahmadi, and Peter Joerg Thomas. On the effect of gravitational and hydrodynamic forces on particle motion in a quiescent fluid at high particle Reynolds numbers. *Canadian Journal of Physics*, 86(6):791–799, 2008.

[11] Pierre Sagaut. *Large Eddy Simulation for Incompressible Flows: an Introduction*. Springer Science & Business Media, 2006.

[12] ANSYS Inc. *ANSYS® Academic Research, Release 16.2, Help System, Coupled Field Analysis Guide, ANSYS, Inc.* Cary, NC, 2017.

[13] Subodh Chander, Ayhan Akinturk, and Bruce Colbourne. Hydrodynamic study of submerged ice collisions. *ASME 2015 34th International Conference on Ocean, Offshore and Arctic Engineering*, 2015.

[14] Hadj Ounis and Goodarz Ahmadi. Motions of small rigid spheres in simulated random velocity field. *Journal of Engineering Mechanics*, 115(10):2107–2121, 1989.

[15] Joseph Kestin, Mordechai Sokolov, and William A Wakeham. Viscosity of liquid water in the range -8 °c to 150 °c. *Journal of Physical and Chemical Reference Data*, 7(3):941–948, 1978.

[16] MATLAB. *version 9.0.0.34 (R2016a)*. The MathWorks Inc., Natick, Massachusetts, 2016.

[17] Manoj Parmar, Allen Haselbacher, and Sivaramakrishnan Balachandar. Generalized Basset-Boussinesq-Oseen equation for unsteady forces on a sphere in a compressible flow. *Physical Review Letters*, 106(8):84–501, 2011.

[18] George Gabriel Stokes. *On the Effect of the Internal Friction of Fluids on the Motion of Pendulums*, volume 9. Pitt Press, 1851.

[19] Rory LC Flemmer and Charles L Banks. On the drag coefficient of a sphere. *Powder Technology*, 48(3):217–221, 1986.

[20] Nicolas Lyotard, Woodrow L Shew, Lydéric Bocquet, and John-F Pinton. Polymer and surface roughness effects on the drag crisis for falling spheres. *The European Physical Journal of Condensed Matter and Complex Systems*, 60(4):469–476, 2007.

[21] Bodo Ruck and Ba Makiola. Particle dispersion in a single-sided backward-facing step flow. *International Journal of Multiphase Flow*, 14(6):787–800, 1988.

[22] Paola Causin, Jean-Frédéric Gerbeau, and Fabio Nobile. Added-mass effect in the design of partitioned algorithms for fluid–structure problems. *Computer Methods in Applied Mechanics and Engineering*, 194(42):4506–4527, 2005.

[23] Fabián A Bombardelli, Andrea E González, and Yarko I Niño. Computation of the particle basset force with a fractional-derivative approach. *Journal of Hydraulic Engineering*, 134(10):1513–1520, 2008.

[24] Renwei Mei, Christopher J Lawrence, and Ronald J Adrian. Unsteady drag on a sphere at finite Reynolds number with small fluctuations in the free-stream velocity. *Journal of Fluid Mechanics*, 233:613–631, 1991.

[25] Eric Loth and Andrew J Dorgan. An equation of motion for particles of finite Reynolds number and size. *Environmental Fluid Mechanics*, 9(2):187–206, 2009.

[26] Nicolas Mordant and John F Pinton. Velocity measurement of a settling sphere. *The European Physical Journal B-Condensed Matter and Complex Systems*, 18(2):343–352, 2000.

[27] Michel Van Hinsberg, Jan HM Boonkkamp, and Hans JH Clercx. An efficient, second order method for the approximation of the Basset history force. *Journal of Computational Physics*, 230(4):1465–1478, 2011.

[28] Junuthula N Reddy and David K Gartling. *The Finite Element Method in Heat Transfer and Fluid Dynamics*. CRC press, 2010.

[29] Gilbert Strang and George J Fix. *An Analysis of the Finite Element Method*, volume 212. Prentice-hall Englewood Cliffs, NJ, 1973.

[30] Richard Courant and David Hilbert. *Methods of Mathematical Physics*, volume 1. CUP Archive, 1965.

[31] Richard Courant. Variational methods for the solution of problems of equilibrium and vibrations. *Lecture Notes in Pure and Applied Mathematics*, pages 1–100, 1994.

[32] Yanping Lin, Jiangguo Liu, and Min Yang. Finite volume methods: an overview on recent developments. *International Journal of Numerical Analysis Model*, 4(1):14–34, 2013.

[33] Yuri Bazilevs, Kenji Takizawa, and Tayfun E Tezduyar. *Computational Fuid-Structure Interaction: Methods and Applications*. John Wiley & Sons, 2013.

[34] Gene Hou, Jin Wang, and Anita Layton. Numerical methods for fluid-structure interaction: a review. *Communications in Computational Physics*, 12(02):337–377, 2012.

[35] Robert D Guy and David A Hartenstine. On the accuracy of direct forcing immersed boundary methods with projection methods. *Journal of Computational Physics*, 229(7):2479–2496, 2010.

[36] Charles S Peskin. The immersed boundary method. *Acta Numerica*, 11:479–517, 2002.

[37] Earl H Dowell and Kenneth C Hall. Modeling of fluid-structure interaction. *Annual Review of Fluid Mechanics*, 33(1):445–490, 2001.

[38] Juan Cebral, Rainald Loehner, and Rainald Loehner. Fluid-structure coupling-extensions and improvements. *35th Aerospace Sciences Meeting and Exhibition*, pages 858–888, 1997.

[39] Roland Glowinski, Todd I Hesla, and Daniel D Joseph. A distributed Lagrange multiplier/fictitious domain method for particulate flows. *International Journal of Multiphase Flow*, 25(5):755–794, 1999.

[40] Hong Zhao, Jonathan B Freund, and Robert D Moser. A fixed-mesh method for incompressible flow–structure systems with finite solid deformations. *Journal of Computational Physics*, 227(6):3114–3140, 2008.

[41] Marcel Lesieur. *Turbulence in Fluids*, volume 40. Springer Science & Business Media, 2012.

[42] Philipe R Spalart and Steven R Allmaras. A one equation turbulence model for aerodynamic flows. *Aerospace Research Journal*, pages 5–52, 1994.

[43] Elijah P Newren, Aaron L Fogelson, Robert D Guy, and Robert M Kirby. A comparison of implicit solvers for the immersed boundary equations. *Computer Methods in Applied Mechanics and Engineering*, 197(25):2290–2304, 2008.